Aalto University
School of Engineering

Jussi Juola

Multi-angular measurement of woody tree structures with mobile hyperspectral camera

Thesis submitted for examination for the degree of Master of Science in Technology.

Espoo 18.07.2019
Supervisor: Prof. Miina Rautiainen, Aalto University
Advisor: PhD Aarne Hovi, Aalto University

Aalto University
School of Engineering

Aalto University, P.O. BOX 11000, 00076 AALTO
www.aalto.fi

Abstract of master's thesis

Author Jussi Juola

Title of thesis Multi-angular measurement of woody tree structures with hyperspectral camera

Master programme Geoinformatics **Code** ENG22

Thesis supervisor Professor Miina Rautiainen

Thesis advisor(s) PhD Aarne Hovi

Date 18.07.2019 **Number of pages** 67 **Language** English

Abstract

Laboratory measurement settings that can acquire spectral and multi-angular information on canopy elements (e.g. leaves and woody tree structures) provide invaluable data for the interpretation and development of forest reflectance models and other optical remote sensing techniques. Previous studies have pointed out that the spectral properties of woody tree structures of boreal tree species have been studied little in comparison to leaves, and that there is a need to fill this gap in knowledge. This thesis presents a custom-built multi-angular measurement system with imaging capabilities that was used to acquire a hyperspectral dataset of boreal woody tree structures of the three most common tree species found in Finland. A total of six trees, two trees per species of Norway spruce (*Picea abies* (L.) Karst), Scots pine (*Pinus sylvestris* L.) and silver birch (*Betula pendula* Roth) stems were sampled at different heights (at every meter of height between 1–10 m) and sides (northward and southward facing sides of the stem), and the stem surface (bark) was measured with a novel mobile hyperspectral camera called Specim IQ. The camera operates in the wavelength range of 400–1000 nm. The acquired dataset contains hyperspectral images of 120 stem samples, each imaged from six different view angles. A designed pixel-by-pixel data processing chain is described. It can calculate and extract accurate pixel specific reflectance information that is invariant to uneven spatial distribution of incident irradiance from the lamp. Finally, the processed data was analyzed to reveal within- and between-species, angular, and spatial variations in stem bark reflectance for the three species.

In concordance to previous studies, this thesis found that the species varied highly in their mean spectra and were distinguishable from one another. In addition, the within-species variation and standard deviation between mean spectra of samples was surprisingly low with very similar spectral signatures between samples of the same species. Investigating angular variation revealed that both pine and birch present strong specular reflections in the forward-scattering angles, in comparison to spruce, which presented a hot spot effect in the backward-scattering angles when measured near the lamp. Birch and spruce showed weak trends when looking at the spatial variations occurring in reflectance due to sampling height or side of the stem. However, pine displayed a clear increase in reflectance from 1 m to 4 m height at 663.81 nm (red band) and from 1 m to 5 m height at 865.5 nm (near-infrared band).

The data obtained in this study show potential for future tasks such as tree species classification and the further development of forest reflectance models. The methods and materials presented in this study can give ideas for developing imaging goniometer systems that can acquire even more information on various vegetation canopy elements than what were presented in this thesis.

Keywords multi-angular, Specim IQ, BRF, goniometer, remote sensing, hyperspectral, imaging spectroscopy

Aalto-yliopisto
Insinööritieteiden
korkeakoulu

Aalto-yliopisto, PL 11000, 00076 AALTO
www.aalto.fi

Diplomityön tiivistelmä

Tekijä Jussi Juola

Työn nimi Puiden runkojen monikulmamittaus kannettavalla hyperspektrikameralla

Maisteriohjelma Geoinformatiikka **Koodi** ENG22

Työn valvoja Professori Miina Rautiainen

Työn ohjaaja(t) MMT Aarne Hovi

Päivämäärä 18.07.2019 **Sivumäärä** 67 **Kieli** Englanti

Tiivistelmä

Laboratorio-olosuhteissa käytettävät mittausjärjestelmät, jotka pystyvät keräämään spektriaineistoa eri mittauskulmista, tuottavat arvokasta tietoa metsien heijastusmallien ja muiden kaukokartoitustekniikoiden tulkintaa ja kehittämistä varten. Aikaisemmat tutkimukset ovat osoittaneet, että boreaalisen vyöhykkeen puulajien puumaisten osien spektriominaisuuksia ei ole tutkittu yhtä paljon kuin lehtien, ja tämän takia kyseiselle tiedolle on selkeä tarve. Tässä diplomityössä rakennettiin monikulmainen kuvantava mittausasetelma, jolla mitattiin hyperspektriaineisto kolmesta Suomen yleisimmästä puulajista: kuusesta (*Picea abies* (L.) Karst), männystä (*Pinus sylvestris* L.) ja rauduskoivusta (*Betula pendula* Roth). Mitattavat näytteet kerättiin yhteensä kuudesta puusta, kahdesta puusta per puulaji. Näytteitä otettiin rungon eri korkeuksilta (metrin välein kymmeneen metriin asti) ja ilmansuunnista (pohjoinen ja eteläinen puoli runkoa). Rungon pintaosan (kuoren) heijastusspektri mitattiin uudella kannettavalla Specim IQ -hyperspetrikameralla, joka pystyy keräämään tietoa 400–1000 nanometrin aallonpituuksilta. Kerätty spektriaineisto koostuu Specim IQ:lla mitatuista hyperspektrikuvista, joita otettiin 120 näytteestä. Jokainen näyte kuvattiin kuudesta eri kulmasta. Mittausasetelman lisäksi tässä diplomityössä kehitettiin pikselikohtainen prosessointimenetelmä, jonka avulla voi laskea näytteen heijastusspektrin siten, että siihen ei vaikuta lampusta epätasaisesti jakautuva valo. Prosessoitujen hyperspektrikuvien avulla tutkittiin, kuinka heijastusspektri vaihtelee puulajien välillä sekä sisäisesti puulajin näytteiden välillä. Lopuksi tutkittiin, kuinka eri mittauskulmat ja näytteenottokorkeus vaikuttavat kuusen, männyn ja koivun heijastusspektreihin.

Yhtenevästi aikaisempien tutkimusten kanssa tämän diplomityön tulokset osoittavat, että puulajien väliset erot heijastusspektreissä olivat suuria ja puulajit toisistaan erotettavissa. Toisaalta puulajin sisäinen vaihtelu oli yllättävän pientä ja saman puulajin näytteiden spektrit olivat samanlaisia toisiinsa nähden. Mittauskulman vaikutuksen selvittäminen osoitti, että männyllä ja rauduskoivulla heijastus suuntautuu voimakkaasti eteenpäin. Toisaalta kuusi osoitti voimakkaampaa taaksepäin valonlähdettä kohti suuntautuvaa heijastusta. Kuusella ja rauduskoivulla oli havaittavissa vähäistä heijastuksen spatiaalista vaihtelua näytteenottokorkeuksien ja ilmansuuntien välillä. Toisin kuin kuusi ja rauduskoivu, mänty osoitti selkeää nousevaa heijastusta 663.81 nm aallonpituudella (punainen kanava) 1 m korkeudelta 4 m korkeuteen. Lähi-infrapunakanavalla (865.5 nm) vastaava kasvu havaittiin välillä 1–5 m.

Tässä diplomityössä kerättyä tietoa on mahdollista käyttää puulajien tunnistusmenetelmien sekä metsien heijastusmallien kehittämisessä. Tämän lisäksi esitetyt koetekniikat ja tutkimusmenetelmät voivat auttaa kehittämään kuvantavia goniometrijärjestelmiä, joilla voisi kerätä vieläkin laajempaa tietoa kasvillisuudesta ja sen eri heijastusominaisuuksista.

Avainsanat monikulma, Specim IQ, BRF, goniometri, kaukokartoitus, hyperspektri, kuvantava spektroskopia

Preface

I wish to take this opportunity to thank my advisor Aarne Hovi for his exceptional guidance and the continuous support he has shown me. I would also like to thank my supervising professor Miina Rautiainen for giving me the opportunity and inspiration to reach my goals. Thank you to the entire Remote Sensing Research Team.

I want to thank Sanna Ervasti and the City of Vantaa for supporting this thesis by donating the trees for scientific research. Without the samples, this study would not have happened.

I also want to extend my thanks to Arttu, Jani, Joonas, Niko, and Mathew for the best two years.

Finally, a big thank you to my family for their endless support and encouragement.

Espoo 18.07.2019

Jussi Juola

Contents

List of symbols

Symbol	Unit	Quantity
E	W m^{-2}	Irradiance
E_λ	W m^{-2} μm^{-1}	Spectral irradiance
F	W	Radiant flux
L	W m^{-2} sr^{-1}	Radiance
L_λ	W m^{-2} sr^{-1} μm^{-1}	Spectral radiance
R	W m^{-2}	Radiant flux density
f	Hz	Frequency
t	s	Integration time
α	unitless	Fraction of absorbed radiation (absorptance)
θ_i	°	Illumination zenith angle
θ_r	°	Sensor zenith angle
λ	m	Wavelength
ρ	unitless	Fraction of reflected radiation (reflectance)
τ	unitless	Fraction of transmitted radiation (transmittance)
ϕ_i	°	Illumination azimuth angle
ϕ_r	°	Sensor azimuth angle

List of abbreviations

ASD	Analytical Spectral Devices, Inc.
BRDF	Bidirectional Reflectance Distribution Function
BRF	Bidirectional Reflectance Factor
CCD	Charge-Coupled Device
CHRIS	Compact High Resolution Imaging Spectrometer
CMOS	Complementary Metal-Oxide-Semiconductor
DBH	Diameter at breast height
DC	Dark Current
DN	Digital Number
FGI	Finnish Geodetic Institute
FIGIFIGO	Finnish Geodetic Institute Field Goniospectrometer
FIGOS	Field Goniometer System
FOV	Field of View
GPS	Global Positioning System
IR	Infrared
LAI	Leaf Area Index
LAGOS	Laboratory Goniometer System
MIR	Mid-infrared
MISR	Multi-angle Imaging SpectroRadiometer
NIR	Near-infrared
PVC	Polyvinyl chloride
QTH	Quartz Tungsten Halogen
RGB	Red-Green-Blue
RSL	Remote Sensing Laboratories
SWIR	Shortwave-infrared
UAV	Unmanned Aerial Vehicle
UV	Ultraviolet
VIS	Visible

1 Introduction

1.1 Background

Spectrometers are devices that are used to measure the properties of light [1]. They are passive optical sensors that can measure intensity of light in narrow wavebands. Spectrometers are one of the core instruments that are used in most ground-based measurement settings when studying optical properties of vegetation. They form a crucial instrument for Earth observation studies. The field that spectrometers represent is optical spectroscopy, which is the study of light (range of electromagnetic radiation) as a function of wavelength that has been absorbed, reflected or emitted from a medium (be it solid, liquid or gas) [1, 2]. The spectral measurements form a graph that assigns a certain amount of reflected or emitted energy for each wavelength in that function [3]. This graph is commonly known as a spectral signature. Spectral signatures are used for large number of measurement solutions, as it is possible to determine what the material is made of and how much of it there is. Spectrometers can capture spectral data from ultraviolet, visible, near-infrared to shortwave-infrared spectrum regions (depending on the device and intended use), covering the full solar reflected spectrum. Spectroscopy is non-destructive and enables the determination of material's properties without altering the measured surface [1]. Spectroscopy is ultimately used to study the interaction of energy and surfaces, enabling us to upscale from leaves (single measures) to entire forest canopies (large-scale measures) [3]. Occasionally, it is possible to find works where the term hyperspectral is used interchangeably when talking about spectrometry and spectroscopy [2]. The term hyperspectral simply defines the instrument to have the capability of measuring large amount of contiguous spectral bands (e.g. hundreds of bands or more). Today, hyperspectral imaging sensors allow the acquisition of data (images) where complete reflectance spectrums are obtainable for each pixel in the image [4]. The sheer amount of information obtainable with imaging spectrometers has the potential to improve our understanding of the interactions of energy and surface materials.

Noteworthy is, that hyperspectral imaging of the Earth is a relatively recent technique for optical remote sensing. It has gained excitement due to the recent technological developments that have allowed for hyperspectral imaging to blossom. The history of hyperspectral imaging is closely tied to the breakthroughs in digital electronics and computing capabilities [5]. Now, thanks to vast developments in technology and innovations produced by related industries, we are seeing a rapid increase in spectral and hyperspectral data available to an ever-growing pool of users. This trend has been predicted to only continue in the near future. Whilst the data flow keeps rapidly increasing, we are facing the challenge of producing meaningful information from the data. Earth observation is the main producer of continuous temporal and spatial spectral data. Continuous data is guaranteed as the amount of satellites as sensor platforms increase rapidly, and hyperspectral imaging devices on board are becoming more common for the collection of surface reflectance values of the Earth below them. However, this puts pressure to produce accurate research on the observable surfaces found in the field that can be used to calibrate and validate remotely sensed data that has been collected by various platforms, be it space-borne or airborne. Previous studies have found that the combination of validation data from ground-based measurements and the remotely sensed data can reduce uncertainty and allow large scale mapping of forest biochemical and biophysical characteristics [6]. Ground-based measurements provide contributions such as: correct remotely sensed images by measuring atmospheric conditions and reflectance of reference ground targets, parameterize forest

reflectance models through inputting optical properties from the entire forest canopy (woody tree structures, leaves, forest floor etc.), and measuring vegetation parameters estimated from remote sensing data (e.g. leaf area index, water content, and chlorophyll content) for independent validation [6]. In addition, there is growing evidence that the data from hyperspectral imaging is potentially extremely valuable for calculating narrowband vegetation indices that can be used to improve the established biomass and leaf area index (LAI) estimates over broadband spectral data [7].

Conventionally in optical remote sensing, reflection measurements have been made from one view angle, usually from nadir (vertically above). However, studies have shown that the spectral signal reflected from any surface material depends on the illumination-view geometry, making it anisotropic in nature. This anisotropy comes from the fact that surface materials are three-dimensional, where size, shape and geometrical arrangement are the key contributors to the variation in directional properties of reflected radiation. Furthermore, scientists have recognized and understood that this angular variation provides valuable additional information about the biophysical and biochemical properties of vegetation [8]. Hence, multi-angular measurement techniques can and should be utilized to measure the spectral anisotropy of vegetation, which in turn can be used for investigating canopy structure and related biophysical characteristics. Additionally, as surface materials are anisotropic in reflectance, multi-angular measurements are also needed for interpreting results obtained from conventional nadir view angle measurements. When considering non-ground-based measurement settings, multi-angular remote sensing data has been available limitedly through airborne measurement campaigns and from multi-angular spaceborne systems such as NASA's Multi-angle Imaging SpectroRadiometer (MISR) or ESA's Compact High Resolution Imaging Spectrometer (CHRIS).

Historically, the spectral properties of woody tree structures of boreal tree species have been studied fairly little when compared to leaves. More so, studies have shown that there are only few public databases available for spectral properties of leaves and woody tree structures of typical boreal forest tree species [9]. Most of these previous studies of spectral properties of woody tree structures have been performed with non-imaging spectrometers and the measured target has been imaged with a conventional photographic camera for possible further visual interpretation.

The Specim IQ is the first mobile hyperspectral camera launched in 2018 [10], produced by Specim, Spectral Imaging Ltd. [11]. Soon after the launch, the camera was studied and evaluated with regards to the measurement quality and performance in vegetation studies [12]. The camera showed possibilities in applications for field and laboratory measurements. Especially when it comes to non-destructive monitoring of plant diversity and other vegetation studies, the flexible and mobile nature of the camera shows a very promising approach. The combination of compactness, mobility and pushbroom imaging technology, create an interesting opportunity for constructing a multi-angular measurement setup that utilizes imaging capabilities, rather than the conventional non-imaging goniometers utilizing point spectrometer technology. As mentioned earlier, each pixel within the hyperspectral image constitutes to a sample with a spectrum, rather than just one graph acquired with the point spectrometer (there are large differences in the amount of information recorded). In addition, the Specim IQ opens the possibility to construct a relatively small, compact and lightweight multi-angular system that is flexible and modifiable. This is shown to be true in this thesis, as it gave an opportunity to build possibly the first multi-angular hyperspectral imaging setup for measuring one of the largest collections of woody tree samples to date. Finally, at the time of this study, there has been

only a small number of studies involving the Specim IQ, and this thesis hopefully gives more insight into the possibilities this novel technology can provide now, and in the future.

1.2 Objectives

The objective of this thesis is to build and test a multi-angular measurement setup for a mobile hyperspectral camera that collects spectral data between the wavelength range of 400–1000 nm. The constructed measurement setup is then used to collect spectral data of woody tree structures from three most common boreal tree species found in Finland. A possible data processing chain is described, and a pixel-by-pixel data analysis method is attempted for precise information extraction. The processed spectral data is then analyzed for measured samples to obtain information on the between-species variations in spectra. Additionally, the objective is to study and analyze the spatial and angular variations of spectra in the measured samples.

2 Literature review

2.1 Electromagnetic spectrum

Electromagnetic radiation is a form of energy that spans a wide range of frequencies and wavelengths. Wavelength, λ, is the distance between contiguous wave peaks measured in meters. Frequency, f, is the quantity of waves that pass a given point in one second, measured in Hertz (Hz) or cycles per second. Alternatively, electromagnetic radiation can be described as being composed of quanta, called photons. There is an inverse relationship between the amount of energy contained in a photon and the wavelength or frequency of electromagnetic radiation. The larger the wavelength, the lower the energy is, and vice versa.

Remote sensing utilizes these frequencies and wavelengths to distinguish and categorize the radiation into an electromagnetic spectrum. The electromagnetic spectrum is divided into regions of frequencies and wavelengths that all contain valuable information with specific use and value for optical remote sensing. These regions are divided by soft arbitrary boundaries, but they are still distinguishable from one another. The spectrum holds accepted regions such as the ultraviolet (UV) between wavelengths of 10 nm to 400 nm, visible (VIS) between 400 nm to 700 nm, and infrared (IR) ranging wavelengths from 700 nm to 1 mm. As an example, the VIS region is the range of wavelengths and frequencies of electromagnetic radiation that the human eye responds to. In addition, the VIS region of electromagnetic radiation contains valuable information for vegetation monitoring. The IR region is often further divided into smaller ranges and described with terms such as near-infrared (NIR), shortwave-infrared (SWIR) or mid-infrared (MIR). The range of wavelengths that are of high interest for investigating plant physiology lie between 300 nm and 15 μm. Electromagnetic radiation from the sun is generally used in optical remote sensing, and artificial illumination from lamps is used when conducting laboratory measurements to provide us with the radiant energy needed to study vegetation in a controlled environment.

2.2 Radiometric quantities

Electromagnetic waves are formed of energy (or quantum) known as radiant energy. Regardless of the source, the radiant power or radiant energy per unit time is called radiant flux, F, measured in watts [W]. The radiant flux that lands (is incident upon) or leaves (emitted from) a unit area of a surface is called radiant flux density, R, and it is measured in watts per square meter [W m^{-2}]. There is also an alternative term for this called irradiance, E, and it is used if that radiant energy is incident on a horizontal planar surface. Furthermore, the radiant flux density or alternatively irradiance, that passes through or is emitted from a unit area of some surface towards a solid angle is called radiance, L, and it is measured in watts per square meter per steradian [W m^{-2} sr^{-1}]. Solid angle is the measure of how large an object appears to the sensor or observer viewing from a specific direction and location (measured in steradian [sr]). Commonly when talking about energy emitted by some natural source, the energy is wavelength dependent, thus the wavelength specific radiance or irradiance is then called spectral radiance [W m^{-2} sr^{-1} μm^{-1}] or spectral irradiance [W m^{-2} μm^{-1}] [13].

Radiant flux that is incident on a surface material is either absorbed or scattered, depending on its wavelength and frequency. If this flux scatters in such a manner, that it is redirected backwards from the planar surface it was first incident upon, it is called a reflection. On the other hand, if the flux scatters and passes through forward to the other side

of this surface material, it is termed as transmission. Absorption of the energy can occur if it enters the interior of the surface material and does not exit from it. An important concept is that all the energy is conserved, even after interacting with the surface material. So, the total radiant flux even after reflection, transmission and absorption equals to the incident radiant flux. This can be expressed with [8]:

$$F_{I,\lambda} = F_{R,\lambda} + F_{A,\lambda} + F_{T,\lambda} \quad (1)$$

where,

$F_{I,\lambda}$ is the incident flux [W],
$F_{R,\lambda}$ is the reflected flux [W],
$F_{A,\lambda}$ is the absorbed flux [W],
$F_{T,\lambda}$ is the transmitted flux [W].

If we then divide this equation with the incident flux $F_{I,\lambda}$, the equation becomes:

$$\frac{F_{R,\lambda}}{F_{I,\lambda}} + \frac{F_{A,\lambda}}{F_{I,\lambda}} + \frac{F_{T,\lambda}}{F_{I,\lambda}} = 1 \quad (2)$$

Which can then be expressed as [8]:

$$\rho + \alpha + \tau = 1 \quad (3)$$

where,

ρ is reflectance of the material [unitless],
α is the absorptance of the material [unitless],
τ is the transmittance of the material [unitless].

In optical remote sensing, devices that are specifically designed for the collection of spectral data, are used to detect and record the interactions of energy and the surface material under investigation. Ultimately, reflectance at different wavelengths (i.e. the spectra) can be used to distinguish between different materials.

2.3 Spectral remote sensing of vegetation

2.3.1 Interaction of electromagnetic radiation with vegetation

The spectral variations in reflectance, especially in the VIS and NIR regions of the electromagnetic spectrum are due to the absorption and scattering of incident solar irradiance (light) at different wavelengths [14]. The mentioned absorption and scattering of incident light are influenced by biochemical properties and biophysical structures of the observed surface [14]. In the case of vegetation, affecting biochemical factors would include leaf pigments (e.g. chlorophyll a and b, and carotenoids) and water content (cell structure) to name a few. However, biophysical structures of vegetation (e.g. orientation and spatial arrangement of elements, and leaf- or plant area indices) also have a substantial effect on absorption and scattering of incident light. In addition to the scattering properties of the

observed surface, atmospheric conditions, object's surroundings and the topography, all affect the reflectance quantities at different wavelengths [13]. Finally, understanding the optical properties of vegetation can be linked to the photosynthetic processes of vegetation [15].

In summary, understanding and quantifying the influence of structural characteristics of vegetation on reflectance can become quite complicated. As a thought, each vegetation canopy has specific size and shape of leaves, leaf orientation and their arrangement are unique, woody tree structures differ between species, and all these together determine the angular distribution of reflected radiance from it.

2.3.2 Multi-angular remote sensing

In order to reliably interpret remotely sensed data (which is directionally dependent), information on these optical properties are needed with the combination of information gained from empirical measurements of surfaces under sufficiently wide range of illumination and sensor view angle geometry (multi-angular measurement setting) [9]. This angular distribution of reflectance can be explored through multi-angular field measurements, laboratory measurements, remotely sensed measurements and modeling studies [13]. The uniting element for said measurement methods is the Bidirectional Reflectance Distribution Function (BRDF), that was determined originally by Nicodemus et al. (1977) [16]. It is the theoretical concept and framework through which the community of remote sensing can discuss reflectance quantities and the anisotropic nature of reflectance. The value gained from modeling this function is that the BRDF of surface targets (how spectral radiation is reflected from the surface) contain information on the composition of the surface that cannot be concluded based solely on the spectral properties [17].

Ultimately, information gathered through measuring this function can be used for validating BRDF models and correcting remotely sensed data, which is of great value especially in satellite-based optical remote sensing. Satellite-based optical remote sensing data can have data sets of the same region but with differing illumination and view angles, and these BRDF models, can be used to improve comparisons through normalizing the data [18]. The reason why data sets can differ in such a challenging way is because of the impact of time, possible changing of seasons (constituting to large variations in sun elevation angle) that produce very different pixel brightness' in the same scene, even when measured by the same sensor [19]. One of the many reasons why correcting remotely sensed data is necessary, is due to the distribution of diffuse irradiance under natural conditions, because there is a direct component from incoming solar irradiance, but diffuse scattering is in addition to this [13]. This means that, as mentioned earlier, the reflectance quantities and spectral distributions are affected by atmospheric conditions, topography and the reflectance properties of the surface [13]. Without correction, the observed quantities do not constitute to the desired true reflectance characteristics of the observed surface.

In summary, focusing research efforts into acquiring spectral and multi-angular information on canopy elements (e.g. leaves and woody tree structures) through field and laboratory measurements, invaluable data can be obtained for the interpretation and development of forest reflectance models and optical remote sensing techniques.

2.4 Bidirectional Reflectance Distribution Function

2.4.1 The concept of BRDF

The BRDF is the ratio of the reflected radiance in a specific outgoing direction to the incident irradiance from incoming light direction [16]. However, this ratio is between infinitesimal solid angles, producing a derivative with angular values existing at a particular instant, that cannot be physically measured [13, 16]. Conceptually, the spectral BRDF [sr^{-1}] evaluates the relationship between the spectral radiance scattered into all directions above a hemisphere of the viewed surface target when it is illuminated from any direction. Mathematically this can be expressed as [13, 16]:

$$f_r(\theta_i, \phi_i; \theta_r, \phi_r; \lambda) = \frac{dL_r(\theta_i, \phi_i; \theta_r, \phi_r; \lambda)}{dE(\theta_i, \phi_i; \lambda)} \quad (4)$$

where,

L_r, is the reflected outgoing spectral radiance [W m^{-2} sr^{-1} μm^{-1}],
E, is the incident (incoming) spectral irradiance [W m^{-2} μm^{-1}],
θ_i, ϕ_i, are the zenith and azimuth angles of incident (incoming) radiation,
θ_r, ϕ_r, are the zenith and azimuth angles of reflected radiation,
λ, is the wavelength.

Hence, the value of the function depends on the given illumination and view angle geometry and wavelength.

2.4.2 Typical BRDF characteristics of vegetation canopy and related elements

A common phenomenon and typical characteristic of BRDF is where the main source of diversity in image pixel values is the so-called hot spot effect. The hot spot effect describes the region in an image that appears to be brighter in pixel values when the direction of the sensor gets close to the direction of illumination (e.g. the sun or a lamp). The hot spot radiance is considered to be the maximum of the distribution in the BRDF model and the minimum can possibly be found in the forward direction of the scattering side (sensor looking at the surface towards the source of illumination) [20]. When the sensor is placed close to the direction of illumination, the sensor sees very minimal amount of shadows because it is looking along the incident rays (hence the hot spot on the backward scattering side) [20]. If the view direction is changed, more shadows are seen, and thus the mean radiance of reflection typically decreases [20]. This is because there is a decreased probability of seeing illuminated particles [20]. This leads to a phenomenon where the anisotropy of the surface reflectance is not due to the changes in the properties of the surface, but due to the changing bidirectional effects of the radiance field around the surface [21]. In other words, the surface material does not change, but instead the illumination-view geometry changes in a way that causes distinct differences in the measured values. As the largest variations in the anisotropy of the surface reflectance (BRDF) occur in the solar principal plane, there is interest and demand to study this bidirectional dependency [22]. Solar principal plane is defined to be the plane at which the sun, sensor and the target surface normal are aligned, along which the hot spot can be found as well [22]. In addition to the hot

spot effect, a similar phenomenon is when specular reflections occur from surface materials. Specular reflection occurs when the surface acts as a mirror (due to having smooth and polished surfaces) and reflects a beam in a way where the angle of reflection is equal or close to the angle of incidence [14]. This again causes very different intensities in measurements. In vegetation, specular reflections are usually observable within single-measures (such as single leaves or other elements) rather than the entire canopy. However, the specular reflections of leaves and other elements do contribute and affect the reflectance properties of the entire scene.

2.5 Multi-angular measurements

2.5.1 Practical concerns with BRDF

As briefly touched on, the drawback with BRDF modelling comes from the fact that if you wish to fully capture and model the BRDF of a specific surface, you must have a source of illumination and a viewing sensor, both with very narrow opening angles, at every direction around the target surface's hemisphere, which cannot be done directly. This is because the function describes infinitesimal differential solid angles that are tied to that function, and sensors can acquire only quantities over a larger viewing angle. It is important to understand the theoretical concept of BRDF, but it is less relevant for practical applications that require a more general expression. Fortunately, for these practical applications, multi-angular laboratory measurements can still be used for exploring the BRDF effect and for validating BRDF models through approximating these bidirectional reflectance quantities [17]. Simply put, through multi-angular measurements at different viewing and illumination angles, it is possible to model and explore the conceptual function through approximations of measurable quantities.

2.5.2 Measurement geometries

Multi-angular measurements can bring us closer to the conceptual reflectance quantities, that in turn can be used to calibrate and correct remotely sensed data. With multi-angular measurement settings, the geometry must be considered thoroughly to report findings accurately. Originally, Nicodemus et al. (1977) [16] defined nine standard reflectance geometries that described the possible combinations of directional, conical and hemispherical domains. The original nine standard reflectance geometries held conceptual and measurable reflectance quantities and were grouped accordingly.

As conceptual quantities are unmeasurable (because incalculably small light sources and sensor field of views do not exist), actual measurements are done under the conical or hemispherical view-illumination geometry [13]. Noteworthy is that, small collimated light sources can be found, but the more substantial problem is obtaining a sensor with an extremely narrow field of view. The basic geometrical setting for all reflectance measurements is conical [16]. However, it is common in practice to assume conical geometry (if small enough) to be directional for calculations, modeling and for reporting measured quantities [17]. Worthy of mention is that, the larger the angular change is within the conical geometry, the larger the error will be. It is a factor that needs to be taken into consideration when e.g. designing measurement setups.

When conducting a practical measurement campaign, each observation in the measurement setting will be conducted under one of the mentioned geometric domains, depending on the illumination and view angle conditions present. This is important to remember, because different illumination and view geometries in practical measurements, are defined with a reflectance factor. In this thesis, due to the later defined and used beam

geometry of the incident and reflected radiant fluxes in the measurement campaign, Bidirectional Reflectance Factor will be used.

2.5.3 Bidirectional Reflectance Factor

Bidirectional Reflectance Factor (BRF) is the ratio of the radiant flux reflected from a target to the radiant flux that would be reflected from a Lambertian surface (diffusely reflecting surface) for the same illumination-view angle geometry and wavelength [13, 16]. For example, the BRF value for a Lambertian surface would be one for all illumination and view directions. This is because Lambertian surfaces reflect light (radiance) equally into all directions and are diffuse by nature. However, Lambertian surfaces described theoretically do not exist in real life. Therefore, perhaps an easier interpretation for practical measurements is that it is the radiance from a target surface divided by the radiance from a white diffuse surface, such as a commonly used white reference material called Spectralon® [23, 24]. In remote sensing, Spectralon® white reference standards are assumed Lambertian and a good approximation for it. The Spectralon® diffuse reflectance material is reported to have 99 percent reflectance (calibrated individually in a laboratory), being the highest of any known material in the world within the spectrum range of UV, VIS and NIR, and have angular characteristics close to Lambertian [25]. Being close to Lambertian means it can maintain constant reflectance properties over a wide range of lighting conditions.

To relate the BRF measurements with the conceptual BRDF, the possibility of conducting measurements at different viewing and illumination angles is required. This is because the BRF describes the anisotropy of reflectance from a surface illuminated from a single direction. Noteworthy for practical measurements of BRF, is that it is defined for small conical solid angles which makes it a measurable quantity, in comparison to BRDF that has infinitesimal solid angles.

In conclusion, to obtain the complete BRDF of the surface, one would need to capture a vast directional sampling combination around the hemisphere of the target surface. The practical question then is, how is it possible to measure reflectance from multiple angles while registering the geometry. In short, it is possible with different kinds of laboratory devices such as goniometers, that have a large enough sampling possibility. This thesis will later present a sample of modern state-of-the-art multi-angular measurement settings.

2.6 Instruments for capturing spectral quantities

2.6.1 Non-imaging spectrometers

Ground-based spectrometers are divided commonly by imaging and non-imaging capabilities. Non-imaging spectrometers, or point spectrometers, are instruments that measure the intensity of the electromagnetic radiation falling within the detectors field of view, within its operating spectral range. A point spectrometer integrates the radiation that arrives at a certain wavelength for the area it sees. As the descriptive name suggests, point spectrometers do not produce images, but rather graphs of intensities at specific wavelengths integrated over the measured surface. Additionally, it is common that a point spectrometer is attached to an integrating sphere that then allows for the measurement of directional-hemispherical reflectance or transmittance.

As an example, if the device collects 2048 bands (contiguous spectral intervals between 350–2500 nm), the output data would consist of 2048 separate measured quantities for the viewed surface area. Ground-based non-imaging spectrometers usually have a high spectral resolution and are used to measure the reflectance spectrum of vegetation species and other material targets. Well-known producers of point spectrometers (e.g. field portable

point spectrometers) that are widely used around the world for remote sensing purposes are Analytical Spectral Devices, Inc. (ASD) (part of Malvern Panalytical Ltd.) [26], Spectra Vista Corporation [27], Spectral Evolution Inc. [28], and Ocean Optics, Inc. [29]. Many studies incorporate instruments by well-known producers, which in turn allows researchers to compare results (comparative research).

2.6.2 Imaging spectrometers

2.6.2.1 Data acquisition with imaging spectrometers

Imaging spectrometers are instruments that are slightly more complex in data acquisition than the above described point spectrometers. With hyperspectral imaging, hundreds of narrow contiguous bands are obtained for an imaged surface, in which, each pixel contains an individual spectrum of the surface covered in that specific pixel. The data collected with a hyperspectral imaging device is commonly visualized as a data cube [2]. It depicts the mentioned spatial and spectral relationship, where the imaged surface will have as many image layers as there are wavelength bands. The cube is used for illustration purposes to visualize the high-dimensional properties of each acquired hyperspectral image. As an example, if an obtained image has the size of 512×512 pixels, and there are 204 spectral bands in the range of VIS–NIR, there will be 204 values assigned for each pixel in the image, making a total of 53 477 376 measured quantities for the entire imaged surface area. The 204 values assigned for each pixel is determined by the established spectral resolution of the imaging sensor (204 bands in said example). In the past, the large quantities of data were a problem for analysis, but the recent developments in image-processing methods can now handle them efficiently and make nearly full use of all the valuable information obtained. A great advantage of imaging spectrometers is also the advantages gained from photographs, as it is possible to visually select and inspect surfaces and targets of interest. This advantage possibly allows for greater opportunities for material classification and vegetation mapping [4]. For remote sensing purposes, imaging spectrometers can be mounted on airborne, spaceborne and ground-based systems, making it very versatile in possible applications. Some well-known producers of hyperspectral imaging cameras and systems are Specim, Spectral Imaging Ltd. [11], Cubert GmbH [30], and Bruker Optics [31].

Imaging spectrometers build the data cube during data acquisition phase in a few different ways, depending on the technology they use. Conventionally, the most common methods for data acquisition is either having a whiskbroom scanner, or a pushbroom scanner [2, 8, 32], two of which this thesis will be describing in more detail. The pushbroom sensor technology has been the standard data acquisition method for many years (i.e. in large airborne imaging spectrometers) and is still applied to state-of-the-art imaging sensors [33]. The whiskbroom sensor technology is another standard method that has been used for many years and helps to understand the versatility and the technology behind imaging spectrometers. For example, because of the ability to quickly scan points on a surface with whiskbroom technology, first attempts have been made to utilize low-cost whiskbroom sensors for Unmanned Aerial Vehicles (UAV) [33].

The word scanner describes the process of data acquisition quite well, because rather than capturing an instantaneous image, it proceeds to scan the observed area. The scanner builds the data cube line by line, in a slightly different way whether it is implementing a whiskbroom (across-track, where series of pixels are collected) or a pushbroom (along-track, where lines of pixels are collected) scanner. These line arrays simultaneously sense each pixel in as many spectral bands as there are detector elements in the line array, making it the core element of the imaging sensor [4]. Imaging spectrometers are developing continuously,

and the complexity of the field has increased rapidly. This has also led to the development of rapid growth in terminology and classification of imaging systems.

2.6.2.2 Pushbroom scanners

Pushbroom scanners collect lines of pixels, along the trajectory of movement. It is common that these pushbroom scanners operate without any mechanical scanning components for the data acquisition [2]. This is the case especially for larger pushbroom scanners in airborne or spaceborne applications where the formation is reliant on the forward movement of the sensor and platform. However, the sensor can be implemented also so that the forward movement of each scan line is done with mechanical components (e.g. a motor) "pushing" the collected line of pixels forward to its next location [12]. The scan lines are a series of one-dimensional samples that are orthogonal to the scan direction [2], and the pushbroom process builds the spatial dimension by scanning the surface and forming the two-dimensional image of pixels [8]. The spectral composition of the image is completed with the line of detectors that detect the energy from one collected scan line. Each individual detector, typically Charge-Coupled Devices (CCD) are used as detectors that measure the energy [8]. The reason why CCDs are used in pushbroom scanners, is that they are sensitive and can be made small in size as well. The disadvantage with CCDs in pushbroom scanners, is that even though they are very sensitive, they can only detect wavelengths in the VIS and NIR [8].

2.6.2.3 Whiskbroom scanners

Whiskbroom scanners typically have the property of scanning the observed surface by some mechanical angular movement. An oscillating mirror that sweeps the line from one edge of the swath to the other covers the field of view [2, 8]. In a whiskbroom scanner, there is typically only one single spatial pixel with corresponding spectral properties, which is rotated along the scan line. In comparison to the pushbroom scanner, the image lines are formed by scanning that single pixel across-track and then the complete image is created again through the forward movement of the platform that holds the sensor. Perhaps the biggest distinction between the two is that pushbroom imaging spectrometers have a one-dimentional field of view, in comparison to the zero-dimensional point-like field of view in whiskbroom imaging spectrometers [32]. Few of the main reasons why whiskbroom scanners are commonly used in imaging spectrometers, are that the single detector line array used in the system produces better spectral uniformity and it allows the optical design to fit a larger detector pixel size [2]. Even though the single detector system is much easier to calibrate than with other systems (i.e. pushbroom scanners), a disadvantage with this principle is the mechanical rotation, which affects the image forming geometry significantly. Since the sensor requires moving parts, it is typically larger than a pushbroom scanner which in turn does not conventionally have any moving parts.

2.7 Multi-angular measurement facilities

2.7.1 Overview of presented facilities

Three multi-angular measurement facilities or systems were chosen to be presented. The chosen three represent a subset of systems operating around the world based on slightly differing technologies, but ultimately striving for the same outcome. The purpose is not to present all known systems, but rather describe typical solutions for multi-angular systems. Nevertheless, the chosen examples represent some of the most innovating technical solutions and even standardized ideas of how goniometers should be built or improved upon. In

addition, the chosen three facilities or systems have been shown to work extremely well for research purposes in many publications. Finally, the facilities or systems will be presented in a chronological order of publication, as there is a mixture of old and new among the systems.

2.7.2 University of Zürich

The Remote Sensing Laboratories (RSL) at University of Zürich have developed and published a field goniometer system called the FIGOS and its laboratory setting counterpart LAGOS (2003) [34, 35]. They are the same system with two different operational settings. At the time of FIGOS' publication [34], it was reportedly the only known system in operation which is capable of simultaneous measurements of the reflected and incident radiances at the same high spectral and angular resolution. For the purposes of this thesis, the LAGOS will be summarized in more detail due to its laboratory measurement setting. Few examples of studies conducted using this system include: comparison of field and laboratory multi-angular measurements [36] and measuring the directional reflectance properties of snow [37].

Shortly about the FIGOS, it is a large goniometer with a radius of 2 meters and built of a zenith and azimuth arcs made of coated aluminum. It is possible to transport it with a standard size van due to the possibility of separating the two arcs. Getting it operational takes reportedly less than 2 hours for a crew of two people. It has a spectroradiometer (GER3700 or an ASD FieldSpec 3 Spectroradiometer) and a laser pointer (to show the center of the field of view) mounted on it.

So, the LAGOS is based on the presented FIGOS, but instead of operating outdoors, it is facilitated inside a darkroom with artificial illumination provided by a 1000 W Quartz Tungsten Halogen (QTH) lamp on a separate adjustable stand. QTH lamps are often used in reflectance spectroscopy because they provide a stable output in the visible and near-infrared wavelengths that is a good approximation of the solar irradiance provided by the sun [38]. The described darkroom is used to minimize scattering and possible stray light. The used spectroradiometer is from the ASD FieldSpec series that operates within a wavelength range of 350–2500 nm. A spectroradiometer is a point spectrometer that has been calibrated spectrally and radiometrically [33]. For laboratory setting, the system has been elevated from the floor to enable the measurement of difficult targets such as entire living plants or other large targets. The advantage of the LAGOS is that it is independent of weather conditions, it has a highly stable and constant illumination and, because of the darkroom, has negligible atmospheric disturbances.

For LAGOS, the distance between the lamp and the target is approximately 1.8 m. Each point on the target is illuminated slightly from a different direction due to the short distance. This system also uses a Spectralon® white reference standard. A full hemisphere measurement (66 measurements, at 15-degree zenith and 30-degree azimuth angle resolution) can be covered within 15 to 20 minutes (in comparison to the reported 25 minutes with FIGOS). A very similar small compact arc-based goniometer (1.25 m arc diameter for light and 1.05 m arc diameter for spectroradiometer), called CLabSpeG, has been developed by Biliouris et. al. (2007) [39], that is also developed for the measurement of vegetation elements such as woody tree structures (bark), soil and leaves.

2.7.3 Finnish Geodetic Institute

Suomalainen et al. (2009) at the Finnish Geodetic Institute (Finnish Geospatial Research Institute since 2015) (FGI) have developed and published a device called the Finnish Geodetic Institute Field Goniospectrometer (FIGIFIGO) [40, 41] for performing ground

based BRF measurements. The goniospectrometer is more commonly called just a goniometer, but the term describes the ability to mount a spectroradiometer sensor and the ability to change its view direction with well-defined angles. Even though it is operational in field conditions, it can be facilitated inside a laboratory as well. The FIGIFIGO operates along a common setting where the sensor moves around the target in the center and measures the same target surface. This device is described to be automated and portable, able to measure in field with sunlight or in the laboratory using an artificial light source such as a 1000 W QTH lamp. Mentioned advantages of the FIGIFIGO is its light design (weighing at 30–40 kg), long operational time (4–8 hours) and the measurement of full hemisphere of BRF (approximately 200 measured spectra) takes 10 minutes. Few examples of studies conducted using the FIGIFIGO: validation of remote sensing data obtained from airborne measurements (e.g. UAV captured data) [42], multi-angular measurement of forest understory species [43], and computing land surface albedos [44].

The main components of the measurement setup include the casing, a measurement arm, a computer and a sunphotometer, which is on an external tripod. The casing contains an ASD FieldSpec Pro R spectroradiometer that operates between 350–2500 nm wavelengths, various electronics and batteries. The rotation of the telescopic measurement arm can be controlled using the computer, with which it is possible to control the measurement zenith angle. The incorporated inclinometer inside the arm allows the controlling. The reach of the telescopic arm is between 1.55–2.65 m. Top of the arm, there are various optics that view the measured surface through a servo-driven mirror. The mirror is there to allow the computer to stabilize the spectrometers FOV with regards to the sample. If used in-doors in a laboratory setting, the artificial illumination used is a 1000 W QTH lamp. A Spectralon® white reference panel is used as the diffuse Lambertian surface for BRF calculations.

2.7.4 Wageningen University

Roosjen et al. (2012) at Wageningen University have published a laboratory goniometer facility formed by a commercially available robotic arm [17]. The arm enables the recording of large number of BRF measurements over the full hemisphere within a short time interval. It can acquire multi-angular reflectance measurements of soil, leaves and small canopies under operator defined illumination conditions. Main advantage of the robot system declared by the authors is its speed, as it is reportedly much faster than other goniometers, and it can be equipped with many sensors including thermometers. In addition to being able to carry spectroradiometer and a thermal camera, it is possible to adjust the measurement distance depending on the zenith and azimuth angle. Few examples of various studies that have been conducted with this system in the Wageningen University goniometer facility include publications such as: investigating soil moisture effects on reflectance anisotropy [45], investigating BRDF effects with multi-angular laboratory measurements [46], and measuring sand moisture effects on spectral reflectance [47].

The goniometer system is facilitated by a Kawasaki FS10E [48] commercially available industrial robot that is programmable to reach an extremely high rate of sampling around the hemisphere due to six movement axes and a large working radius. They report that on average, taking a measurement and moving to the next position takes around 10 seconds. Common setting for commencing measurements around the hemisphere around the surface, is to measure view zenith angles from -90 degrees to +90 degrees off nadir. The radius of the hemisphere can be chosen from 25 cm up to 100 cm. Measurements can be done close to the hot spot where illumination and view angle fall in line. The robot can be programmed to get close to the hot spot, but still so that it does not cast a shadow by being

in front of the illumination source and between the measured surface. The robot allows for a very flexible system with programmable positioning, and operations can be conducted using a computer.

Illumination in this setup was done with an artificial light source, a focus beam 1000 W QTH lamp to be exact. The authors suggest a future study by improving the illumination with a collimator.

Spectral reflectance measurements in this system are conducted with an ASD Fieldspec 3 spectroradiometer. The sensor can acquire reflectance and radiance measurements in the range of 350–2500 nm.

In a laboratory setting, it is important to try to avoid unwanted scattering and stray light, which might influence the measured reflectance. In this system the walls of the laboratory were covered with wall panels painted with black latex. In addition to the wall panels, the floor and the ceiling were covered with black PVC foil. The used foil and latex have a reflectance of less than 3 percent in the visible and NIR as reported in the study.

2.8 Woody tree structures

Even though the significance of collecting ground-based data for materials is well recognized, a recent study found that spectral properties of woody tree structures, especially of boreal coniferous trees, have been researched little, when compared to leaves [9]. As one might think, for forest canopies, the spectral signatures and measured quantities can be distorted by the presence of woody tree structures, the structure of the canopy and the surrounding understory beneath [49]. Ignoring the contribution of woody tree parts may lead to less accurate models and estimates (e.g. estimates of chlorophyll that can be retrieved using imaging spectroscopy) [49]. Studies have shown that the incorporation of woody tree structures at different scales in radiative transfer models decrease the total canopy reflectance and therefore is a significant element to take into consideration for accurate retrieval of biochemical and biophysical properties of vegetation [50]. Additionally, it has been concluded that the reflectance of bark is significantly variable between species, and is similar in reflectance to soil, which increases monotonously from VIS and NIR [9]. This high variation between species and few studies conducted ultimately means that more effort should be placed into studying the optical and structural properties of woody tree structures.

Rautiainen et. al. (2018) [9] found three public databases and listed them in 2018, that contain bark spectra for some coniferous species and a few deciduous species from the Boreal and Hemi-Boreal biomes. From these public databases, it was summarized that for some of the species, NIR reflectance is high and some chlorophyll absorption can be observed at around 680 nm, but even these properties become less clear as the woody tree structures become older [9]. The general difference between woody tree structures (e.g. bark) and leaves, is that leaves show clear chlorophyll absorption in VIS (680 nm region), they display the strong red edge effect, and have high reflectance in NIR. Additionally, it has been reported that especially for coniferous species, the most notable feature that changes when comparing needles to woody tree structures is the decrease in magnitude of NIR reflectance [51]. A similar trend has been observed to happen in the VIS region around the “green peak” at around 550 nm [51].

As established earlier, spectral properties of leaves have been studied more than woody tree structures, but they both lack studies that consider the angular variation on reflectance characteristics. There are only a few studies published on the BRDF measurements of leaves, which have been made with point spectrometers [39, 52]. These studies highlight the topic that leaves should also be seen as anisotropic surfaces (rather than diffuse or Lambertian) that have specular and diffuse reflectance properties which in turn

should change our views on leaf optical properties [52]. At the time of writing this thesis, the author could not find publications on BRDF measurements of woody tree structures.

In conclusion, it seems to be rare and uncommon to find studies that utilize multi-angular measurements and which study BRDF effects of leaves and woody tree structures. Especially when it comes to woody tree structures, there are few to none BRDF measurements conducted. These could be considered as gaps in our knowledge.

3 Materials and methods

3.1 Overview of measurements and data processing

To acquire the spectra of woody tree structures and test the theory and concepts of reflectance anisotropy presented earlier, a novel multi-angular measurement setup was constructed and used in an extensive measurement campaign. The campaign measured samples of Norway spruce (*Picea abies* (L.) Karst), Scots pine (*Pinus sylvestris* L.) and silver birch (*Betula pendula* Roth) stems with Specim IQ mobile hyperspectral camera. In addition to the hyperspectral imaging, high-resolution RGB images of samples were collected with a Nikon D5000 camera. Finally, the hyperspectral images were analyzed with a pixel-by-pixel data processing chain developed with Python programming language.

3.2 Measurement setup

3.2.1 Multi-angular system

The core of the multi-angular measurement setup for this study was the constructed system that allowed the collection of repeatable multi-angular measurements. For field and laboratory measurements, there are many possible alternatives for obtaining multi-angular reflectance data, as we could see from the multitude of different kinds of facilities around the world presented in the literature review in this thesis. However, two main strategies are commonly applied. One is the rotation in azimuth direction and the other alternative is the rotation in zenith direction. In this study, measurements were conducted using a constructed goniometer system that was limited to rotate 180 degrees around the target (-90 and +90 degrees of nadir), along the principal plane only. The reasoning behind using the principal plane only, was that BRF varies the most along that plane, and it was a direct solution for restricting the number of measurement angles for this pilot study. In addition to considering the angular rotation, extensive planning had to be made to assure that the entire system can facilitate e.g. the sensors, designed view-illumination geometry, and repeatable measurement capabilities.

The table, or the base of the system, was an optical honeycomb Nexus breadboard manufactured by Thorlabs, Inc (Fig. 1). The breadboard is specifically designed for photonics, imaging and microscopy applications. An optical table or a breadboard offers an excellent platform for building measurement setups due to the standard M6 (metric threading) holes that are placed throughout to the edge of the tabletop. The holes allow mounting of various instruments, construction pieces and other accessories if needed. The design of the optical tables and breadboards allow for a symmetrical construction and setup. The size of the breadboard in this study was 600×600×60 mm.

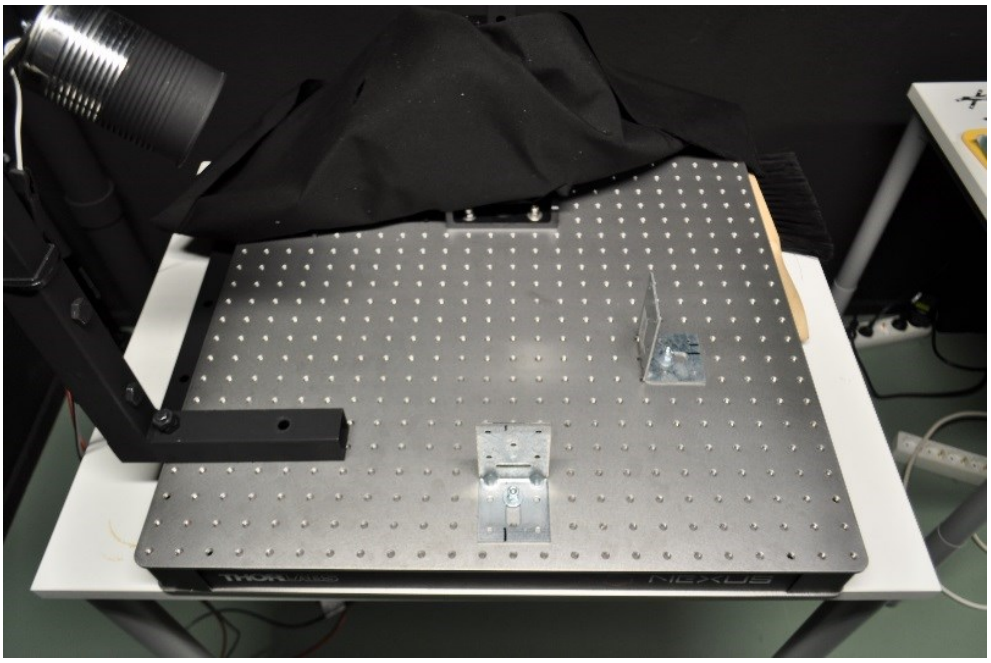

Figure 1. Optical honeycomb breadboard (Nexus model, manufactured by Thorlabs, Inc.) used as the table or base of the constructed measurement system.

The goniometer arm that rotated 180 degrees around target, was constructed out of sturdy square steel piping (size 30×30 mm). The arm was combined with a square steel L-shaped bar where the imaging sensors can be attached to the end of it (Fig. 2). The L-shaped bar was slightly larger than the steel piping of the arm (size 35×35 mm), which allowed it to be placed over the arm piping. The L-shaped bar had 10mm holes that were used to attach it to the arm with bolts and make the mounting of the sensor to the system stable. The arm was machined with compatible holes that enabled the L-shaped bar to be moved up or down along the arm with 10 cm intervals, between 20 and 90 cm height from the fixed axis of rotation. The L-shaped bar that extended away from the rest of the arm, allowed the sensor to be placed and rotated behind the source of artificial illumination. This helped with getting the sensors as close to the hot spot as possible. The arm was attached with a Wixey WR300 Type 2 digital angle gauge that displayed 0–180 degrees in relation to the horizontal base. The gauge allowed for a 0.1-degree resolution for setting the correct angle for measurements, with a 0.1-degree repeatability.

Figure 2. The goniometer arm combined with an L-shaped bar with attachment possibility for sensors at the end of it. Machined holes at 10 cm intervals visible in the picture allowed the measurement height to be adjusted if needed. Small square apparatus attached to the side of the arm was a digital angle gauge.

The arm could be mechanically rotated over the base with manual labor. This was obtained by attaching the arm with an axis between two large right-angle brackets (Fig. 3) that are commercially available as mounting adapters for the Nexus optical honeycomb breadboard (manufactured by Thorlabs, Inc.). The brackets also had multiple tapped M6 holes that allowed the axis height to be adjusted to different heights. The axis height for the arm was set to be 9 cm for this study.

Figure 3. Mechanical rotation with manual labor was obtained with creating an adjustable turn-axis point with the help of two large right-angle brackets (produced by Thorlabs Inc.).

3.2.2 Specim IQ

Specim IQ is based on a line scanner that performs the hyperspectral measurements with the established pushbroom principle described in Section 2. The camera utilizes a motor for the movement of optics [12]. It is capable of capturing spectral data between the wavelengths of 400–1000 nm. The camera itself captures a square image with a resolution of 512×512 pixels, and the two-dimensional image layer is obtained with a static number of 512 imaged lines [12]. Spectral resolution of the Specim IQ is 7 nm with a total of 204 contiguous spectral bands across the 400–1000 nm wavelength range. The entire data cube produced by the camera is therefore 512×512 pixels × 204 bands. The spectral camera in Specim IQ uses complementary metal-oxide-semiconductor (CMOS) sensors [12], rather than CCD sensors that were described briefly in Section 2. In addition, the camera has a field of view of 31 degrees with a minimum measurement distance of 15 cm [12]. In addition to just aforementioned image capturing capabilities (Table 1), the Specim IQ camera can also be used to process data, perform image classification, and visualize classification results as one stand-alone computing unit, if needed [12].

Table 1. Technical specifications for the Specim IQ hyperspectral camera. [12]

Sensor	VIS–NIR 400–1000 nm (CMOS)
Dimensions	207×91×74 mm (depth 125.5 mm with lens)
Weight	1.3 kg
Spectral resolution	7 nm
Spectral bands	204
Image resolution	512×512 pixels
Field-of-view	31×31 degrees
Working distance	150 mm -
F/number	1.7

3.2.3 Nikon D5000

The Nikon D5000 was used in this study to image all samples identically to the Specim IQ camera. It was used to capture high-resolution RBG images for better visual representation of each sample. As a comparison, the Specim IQ produces images of 512×512 pixels, and a typical JPEG image with the Nikon D5000 is 4288×2848 pixels.

3.2.4 Reference targets

The white reference used in this study for the final measurement campaign was a calibrated 10-inch Spectralon® Diffuse Reflectance Target produced by Labsphere Inc. In addition to the larger panel, this study used 1.25-inch Spectralon® Diffuse Reflectance Standards (produced by Labsphere Inc.) as measurement samples. The standards offer diffuse reflectance values that are spectrally flat over the UV-VIS-NIR spectrum. The standards can be bought from a wide range of 2 to 99 percent [23]. This study used standards with nominal reflectance values of 2, 10, 20, 50 and 99 percent. The standards have been calibrated in a laboratory and came with calibrated data between 250–2500 nm. These samples were used for comparison and verification purposes.

3.2.5 Artificial illumination and powering

When conducting optical spectral measurements in a laboratory, it is important that the artificial illumination would have a similar spectrum as what the solar radiation provided by the sun would have outdoors [53]. Quartz Tungsten Halogen (QTH) lamps are a popular option, because they have a good output stability and they provide a smooth spectral output curve, similar to the Sun's. In addition, the advantage of QTH lamps is their intense VIS-NIR spectral output with minimal UV emission. QTH lamps can be found in various power levels, ranging from the 20 W option that is for users and application who do not need high intensity spectral lamps, all the way up to 600 W and 1000 W options that are for high power research needs. It is the specific user and application requirements that ultimately decide what QTH lamp option is adequate for the performed laboratory measurements. The illumination conditions should be tested and tried to confirm that the measurement needs are met. The artificial illumination for this study was constructed to have a stable power source, bulb base attachment, lamp stand, QTH lamp with a reflector and finally a straylight restrictor (Fig. 6A).

As a general remark, a regulated direct current (DC) power supply is commonly used in laboratory spectral measurements because it outputs constant voltage through high regulation and low ripple and noise. These power supplies that are designed particularly for laboratory use are widely applied for many applications that require powering. Therefore, in

this study, a power supply was needed for the artificial illumination to measure samples under stable lighting conditions. The linear laboratory power supply that was used in this measurement campaign was a Twintex TP3020 laboratory power supply with 0–30 VDC output voltage and 0–20A output current.

The chosen lamp type for this study was a 12 V 50 W QTH halogen lamp with a GU5.3 base that could be fitted on a general halogen lamp holder that fits bases G4, GU5.3 and GY6.35. The holder and lamp combination was powered with the established laboratory power supply with 12 DCV voltage. For this study, two models of 50 W QTH lamps were tested and based on the results one of them was chosen to be used in the actual measurement campaign. The two models that were tested differed in their reflector material: first, one was made out of dichroic and the second was made out of aluminum.

The first model of QTH lamp that was tested was an Osram Halogen Superstar lamp with a 36-degree-wide beam dichroic reflector around the bulb, providing 550 lumens. This lamp had a color temperature of 3000 Kelvins (K). The spectra of this lamp was investigated by calculating the irradiance between 350–2500 nm through radiance measurements with a radiance calibrated ASD FieldSpec 4 spectroradiometer. The equation used for calculating the irradiance can be derived from the equation of BRDF as follows:

$$\mathrm{BRDF} = \frac{L}{E} \tag{5}$$

where,

L is the reflected outgoing radiance observed with the spectroradiometer [W m^{-2} sr^{-1}],
E is the incident irradiance on a Spectralon® white surface target [W m^{-2}].

The BRDF of a Spectralon® white reference target can be expressed as:

$$\mathrm{BRDF}_{\mathrm{spectralon}} = \frac{(R \times \cos(\theta))}{\pi} \tag{6}$$

When measured from nadir, cosine equals one, hence:

$$\mathrm{BRDF}_{\mathrm{spectralon}} = \frac{R}{\pi} \tag{7}$$

where,

R is the reflectance of the Spectralon®,

Finally, we get irradiance from solving E:

$$E = \frac{L}{\mathrm{BRDF}} = \frac{L}{\left(\frac{R}{\pi}\right)} = \frac{L \times \pi}{R} \tag{8}$$

L is measured with the spectroradiometer and it is spectral radiance [W m^{-2} sr^{-1} nm^{-1}]. Integrating E over all measured wavelengths equals to the total irradiance.

The results from testing the Osram Halogen Superstar lamp (dichroic reflector) showed two significant properties. One, the total irradiance was very small (49.94 W m^{-2}) and was only a small fraction of what total irradiance in the summer would be from solar radiation (~500 W m^{-2}) [54]. Two, the VIS-NIR spectral output intensity was also quite low, having a rapid decrease when inspecting NIR wavelengths (Fig. 4). This turned out to be due to the dichroic reflector, which are optimized to project most of the heat through the back of the lamp (typically used in display fittings where objects are illuminated from a short distance and the heat might cause damage), causing most likely the significant decrease in intensity at NIR region.

The second model of a 12 V 50 W QTH lamp that was tested was identical in type as the first one (GU5.3 base, 36-degree beam reflector and 3000 K color temperature), but this model had the beam reflector made out of aluminum. Aluminum reflectors are often recommended to be used for spectral measurements, because unlike the dichroic reflectors, they project most of the heat forwards with the light and provide a smoother and stronger spectrum. The QTH lamp model was a Philips Brilliantline ALU 12 V 50 W (providing 780 lumens). Same irradiance investigation was conducted, and results were compared with the Osram Halogen Superstar. The conclusion was that the aluminum reflector improved the spectrum significantly over the dichroic reflector and the total irradiance measured was much stronger as well (212.164 W m^{-2}) (Fig. 4). The QTH lamp spectra seem to be shifted to the right in comparison to the sun's spectrum, and this is most likely due to the color temperature of both lamps being 3000 K (Fig. 4). Finally, the Philips Brilliantline ALU QTH lamp was chosen to be used in this thesis' measurement campaign.

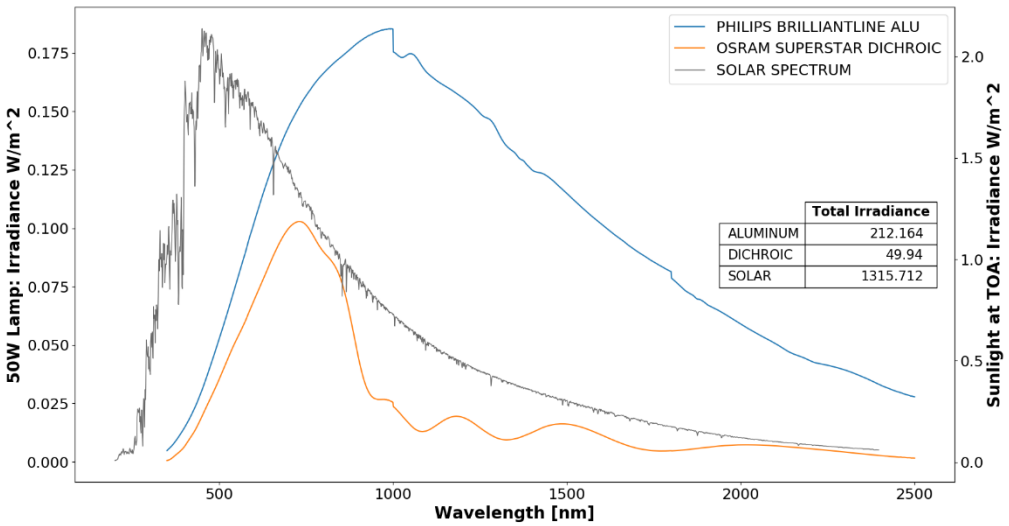

Figure 4. Comparison of spectra between Osram Superstar QTH lamp with dichroic reflector (orange line), and Philips Brilliantline ALU QTH lamp with aluminum reflector (blue line). For reference, the solar spectrum [54] (gray line) is plotted with a separate axis for distribution comparison along the wavelength range of 350–2500 nm. Total irradiance for all three shown in small table.

Another factor that needs to be considered with measurement setups that implement a single fixed source of illumination, is that the distribution of light will not be uniform on the surface of the target. The lamp will illuminate the center of its beam with higher intensity, and then

decreases towards the edges, when the beam is not strictly collimated. This non-uniformity was investigated through hyperspectral imaging the Spectralon white reference target that was illuminated by the Philips Brilliantline ALU QTH lamp (Fig. 5). The results showed that there is an uneven spatial distribution of incident radiant flux. The pixels close to the center of the lamp beam have much higher intensities than the pixels closer to the edge of the beam.

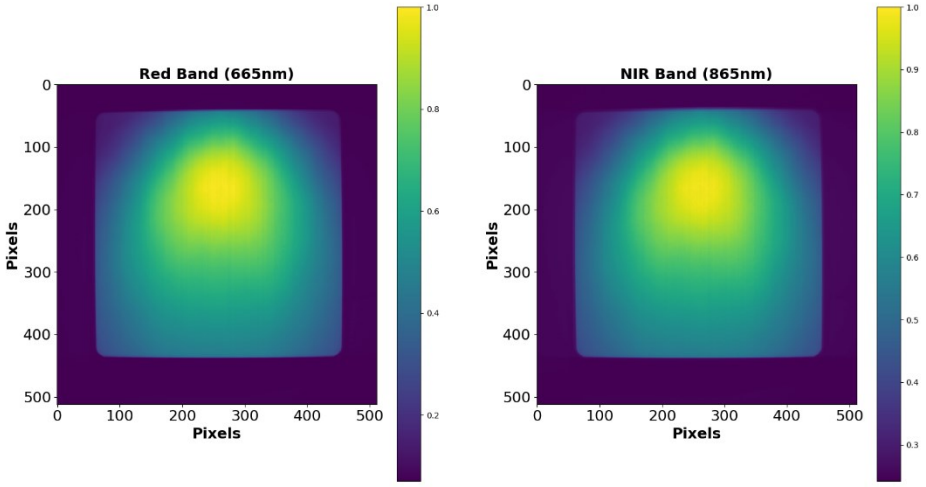

Figure 5. Plots illustrating the uneven distribution of irradiance on a Spectralon white surface target (square object on top of dark background) illuminated by Philips Brilliantline ALU 50 W light source. Plots compiled from hyperspectral images captured with the Specim IQ. Left plot shows the normalized irradiance (maximum irradiance = 1) at 665 nm and the right plot shows normalized irradiance at 865 nm.

After defining the correct lamp and understanding the illumination it provides, the 36-degree beam provided by the manufactured reflector was still too wide. This caused a possible stray light problem that was later realized when direct flares were visible on the sensor lens, affecting the measurement outcomes. The direct beam causing lens flare was of course something that needed to be addressed. This was tackled by building a custom beam restrictor out of an aluminum can, which was cut to fit the lamp inside, and painted in black to avoid specular reflections from the aluminum surface (Fig. 6A). The additional screening restricts the beam from directly causing lens flare on the sensor (Fig. 6B).

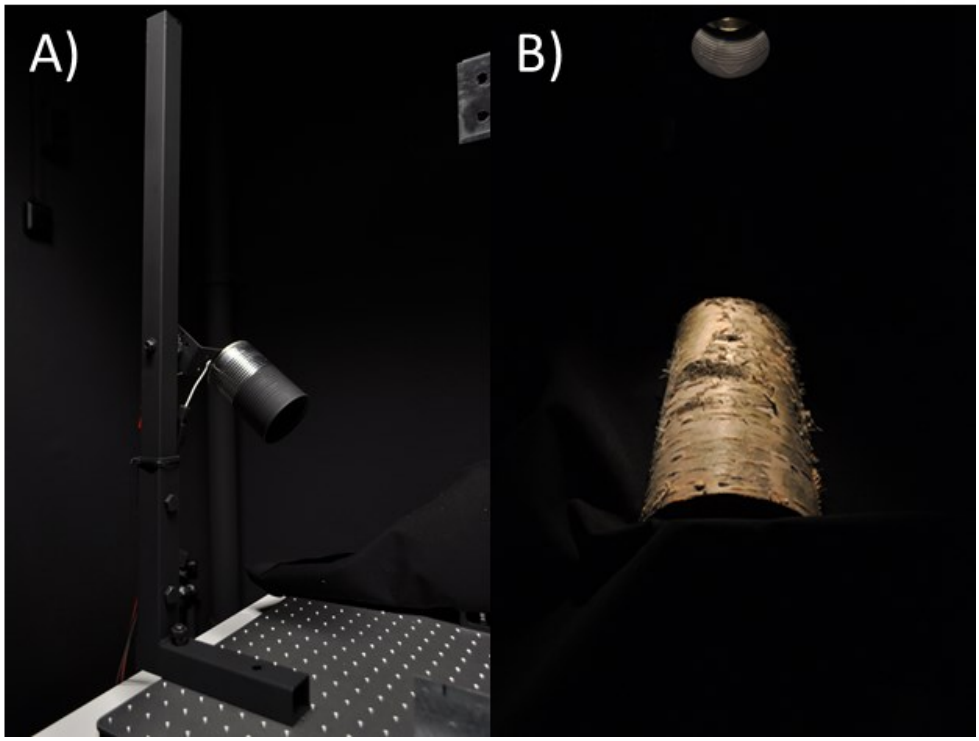

Figure 6. The artificial illumination was constructed to have a stable power source, bulb base attachment, lamp stand, QTH lamp with a reflector and finally a beam focuser (straylight restrictor) (complete system shown in A). The custom beam focuser was constructed to restrict the light beam from directly causing lens flare on the sensor even when measuring from the forward-scattering side (as seen with a sample in B).

3.2.6 Straylight minimization

The measurement setup was mostly constructed using steel and aluminum parts. The problem that arises with the individual parts is that they most likely add error into the data due to possible specular reflections. The measurement setup needed to be coated with non-reflective materials to mitigate the effects of surrounding objects. The arm and lamp holder were spray painted with Nextel Velvet coating 811–21, which is a black special paint that produces a mat and non-dazzling surface. The paint can produce a light-diffusing surface that absorbs >97 percent of the light, independent of the angle of incidence [55]. The base table and the aluminum right-angle brackets were not painted, but instead were covered with black acrylic fiber that absorbs 98 percent of the light (2 percent in directional hemispherical reflectance). In addition to coating the measurement setup, the laboratory room used in this study has been painted with similar black paint. In addition to minimizing stray light with different methods of coating, all measurements were conducted with other external light sources turned off.

3.2.7 Placement of the sample in the setup

A laser pointer was needed to place the sample in the middle of the imaged area. The laser pointer showed the correct orientation and location where each sample should be placed approximately (according to simple geometry calculations). This ensured that the collected images were nearly identical in sample position. The laser pointer was used in conjunction with a tripod to keep it steady and fixed. The laser pointer used had the option to be set as a point pattern, or as a crosshair pattern. Crosshair pattern was used.

The setup base was attached with two right-angle irons to fix the large Spectralon® panel always in the same location with ease and efficiency. The right-angle irons were put at two different sides, so the panel could be just pushed against the two, and it was then fixed in the measured area, viewed by the sensor (irons can be seen in Fig. 1). The right-angle irons were also 9 cm in height, same as what the axis of rotation was fixed at. In addition, the right-angle irons helped with placing the sample in the correct position, together with the laser pointer (Fig. 7).

Figure 7. The multi-angular measurement setup with a sample under investigation. The setup consists of the lampstand integrated with the aluminum beam restrictor with a halogen lamp inside, the multi-angular system with black coating on top, arm lever that can be rotated 180 degrees that also has the sensor attached to it (Specim IQ), laboratory room painted black, a laser pointer and extra curtaining. Actual measurement was done with the external lights turned off.

3.3 Study area and sample trees

The sample trees for this study were donated by the City of Vantaa in Finland. Six trees were donated in total, two of each species: Norway spruce (*Picea abies* (L.) Karst), Scots pine (*Pinus sylvestris* L.) and silver birch (*Betula pendula* Roth). The minimum height for all sample trees was 15 meters. The study area from which the sample trees were collected was located in Keimolanmäki, near the roads Ajolenkki and Varikkokaari (WGS84 latitude 60.3208, longitude 24.8280), in Vantaa Finland (Fig. 8).

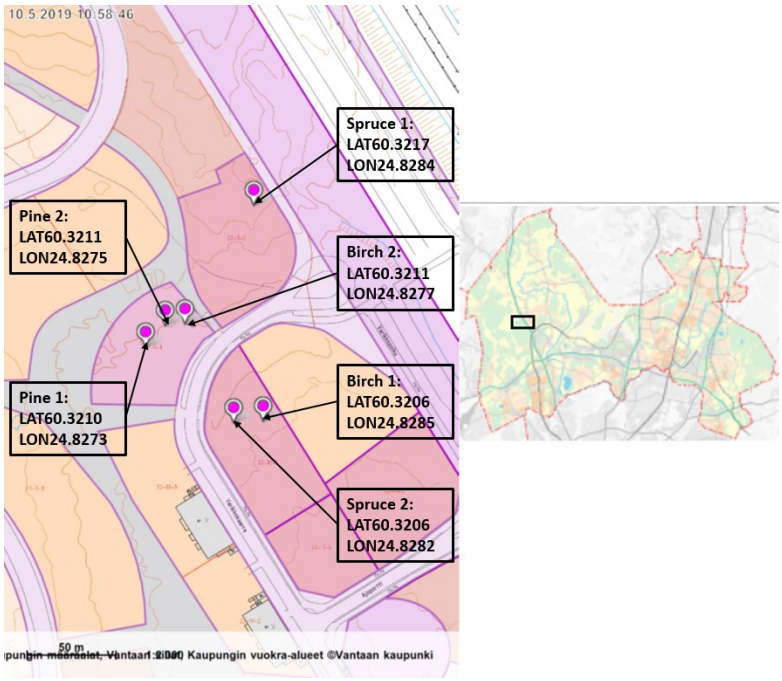

Figure 8. Location of the study area in Vantaa, Finland and coordinates where the six chosen trees (two of each species) were located. Background maps were obtained from the City of Vantaa map service (Copyright City of Vantaa and Sitowise Layers).

Before actual sample collection, two separate visits were made to Keimolanmäki in the beginning of March 2019. On the first visit, the study area was walked through, and an assessment was made about the overall suitability of trees in the area. Preliminary selection of sample trees that fit the sampling specifications were made from the designated plots informed to us by the city officials. The second visit to the study was made together with the city forester, with whom the final tree selection was made and verified with. The selected trees were marked with colored ribbons that could be easily recognized and found later on.

Forest variable measurements were conducted to describe the forests surrounding the selected trees in more detail (Table 2). These measurements included measurement of basal area by angle count sampling (a relascope with basal area factor of 2). The relascope plot was always placed so that the selected tree was at the center of the plot. If the plot surrounding the selected tree was very sparse (e.g. had an open area adjacent to it due to a road), a half measure of angle count sampling was made with the relascope. Height and diameter at breast height (DBH, i.e. 1.3 meters) were recorded for the median tree in the relascope plot. In addition, the coordinates of each selected tree were recorded with a GPS of a cell phone. The tree height was measured with a measuring tape to have a precise result. In addition to the forest variable measurements, panorama photographs were produced (Fig. 9). The dominant tree species within all the plots were Norway spruce, Scots pine and silver birch.

Table 2. Forest inventories for the six selected sample trees.

Tree	Date of collection	Coordinates (lat/lon)	Tree DBH (cm)	Tree height (m)	Basal area (m^2 ha^{-1})	Stand median DBH (cm)	Stand median height (m)
Birch 1	13.3.2019	60.3206, 24.8285	13.5	19.0	22	17.0	21.2
Birch 2	22.3.2019	60.3211, 24.8277	13.5	15.3	24	25.0	16.3
Spruce 1	22.3.2019	60.3217, 24.8284	19.0	17.5	26	25.0	22.9
Spruce 2	14.3.2019	60.3206, 24.8282	19.0	17.2	24	24.5	24.2
Pine 1	22.3.2019	60.3210, 24.8273	20.5	16.9	36	23.0	17.1
Pine 2	22.3.2019	60.3211, 24.8275	13.0	15.2	42	23.5	17.2

The trees were located on a mesic site type. Noteworthy is that the stands were going to be harvested soon by the city because of construction activities planned for the area. This meant that some preliminary harvesting was already made in the study area, where small trees and bushes had been cleared before our measurements (Fig. 9).

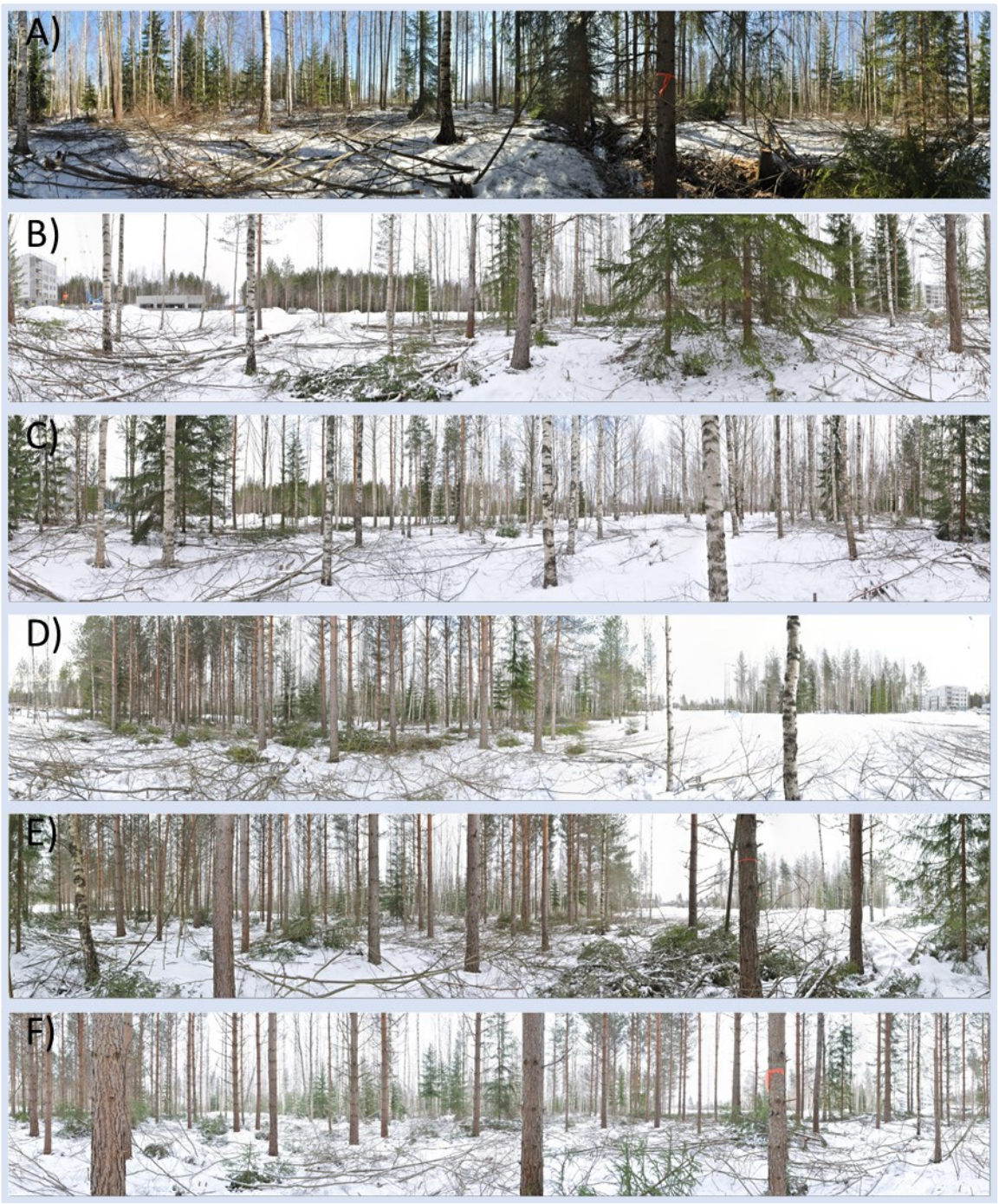

Figure 9. Panorama photographs of forests surrounding the six selected trees: "Spruce 1" (A), "Spruce 2" (B), "Birch 1" (C), "Birch 2" (D), "Pine 1" (E) and "Pine 2" (F).

The labeled tree "Spruce 1" (Fig. 9A) had a large ditch filled with water running right next to it. The tree can be described to been at a shaded location surrounded mostly with deciduous tree species. "Spruce 2" (Fig. 9B) was at a less shaded area than "Spruce 1", being close to a road with few trees between them. The area surrounding "Spruce 2" had a mix of coniferous and deciduous trees.

"Birch 1" (Fig. 9C) was located close to "Spruce 2", but further into the forest plot with more shade and surrounding vegetation. The immediate vicinity was mostly consisting of deciduous trees with relatively sparse distances between them. "Birch 2" (Fig. 9D) was

right along the road and had very little shade and no surrounding trees on the roadside of the plot. The trees next to it were mostly Scots pine trees that dominated the plot.

"Pine 1" (Fig. 9E) was close to the edge of the forest with less shade, similarly to "Birch 2". The surrounding tree species were dominantly Scots pine. "Pine 2" (Fig. 9F) had the same surrounding as "Pine 1", except it was located further into the plot with more shade. However, "Pine 2" had less brush and small trees growing in the close proximity, compared to "Pine 1".

3.4 Collection of samples

3.4.1 Sampling

A total of 120 stem samples were collected from the six trees. For each tree, 20 stem samples were produced, in such a way that for every 1 meter of height (1–10 m from ground), an approximately 20 cm long log was cut. The 20 cm log was then cut in half to produce two samples, one from the southern side of the tree, and another from the northern side of the tree. In addition to providing samples of each species, collecting samples in this manner allows the investigation of possible spatial variations along the height and direction of each tree.

3.4.2 Collection method

Stem samples were collected from the selected six trees through destructive means. Felling and producing correct sample sizes were done with a chainsaw. Each of the six trees were first marked at 1 m height with the main compass coordinates using a Suunto KB-14 hand-bearing compass (Fig. 10A). This was done to keep track of the correct sides of the tree after the tree was cut down. After cutting the tree down, the tree was trimmed of branches (Fig. 10B). After trimming, a measuring tape was laid along the trunk, starting from the 1 m mark produced earlier. For every meter on the measuring tape, a 20 cm sample length was marked, and the compass directions labeled. After labeling was made for the 10 meters along the trunk, the samples were collected. This was done in such a way, that at the lower side of the 20 cm sample mark, the trunk was cut with a chainsaw. The end of the sample that was just cut, was then labeled with the north and south sides (Fig. 10C). After marking the southern and northern sides, the sample was sliced with the chainsaw until the 20 cm mark was met (Fig. 10D). Then another cut was made to produce two samples for that height, one for the south side and another for the north side. The labeling of compass directions were also made to keep track of the growing direction, so that the samples would be placed correctly under the measurement setup. The minimum tree height of 15 m described earlier, was required to get a minimum sample diameter of 5 cm at 10 m height of the tree. The minimum diameter or width of 5 cm was set to ensure that enough pixels of the sample are acquired in the data processing chain.

Figure 10. From left to right: A) marking the compass direction before felling, B) trimming the tree and marking 20 cm samples for every meter up to 10 m height, C) keeping track of north and south sides, and D) finally slicing the 20 cm length log to produce two samples per meter of height.

3.4.3 Storage

The collected samples were stored outside in cool March-April temperatures (approximately between 2–10 °C), covered and protected from weather conditions that could possibly harm or alter the sample's spectral properties in some way. This was mostly in case of rain that might drench the samples with water. Water has very high absorbance, which would potentially be seen in the measurements if the water content of the sample were somehow altered. Another reason why the samples were stored outside in cool temperature was that we did not want the samples to dry to such extent that it might again affect their spectral properties. Measurements were conducted within 12 days from sample collection.

3.5 Measurements

3.5.1 Overview of measurements

The measurements were divided into two categories of multi-angular measurements. The first category was to capture necessary hyperspectral images that are required to calculate the BRF of each stem sample from six different view angles with one fixed illumination angle. The second category was to acquire high-resolution images of each stem sample from the same view-illumination geometry as the first category of measurements. In addition to the stem samples, the established range of Spectralon Diffuse Reflectance Standards were used in this study as samples.

An overview of the measurement setup and used view and illumination angles is provided in Figure 11. Differing from typical goniometer measurements, where zenith angles vary from -90 to +90 degrees, a slightly different angle notation convention was used, to be consistent with typical satellite measurement geometry. In typical satellite measurement geometry, the zero-degree is vertically above the canopy. Consequently, the zero-degree is along the table, towards the "top"-side of the sample (illustrated with arrow and label), because that is where the top of the canopy would be (Fig. 11).

Illumination angle chosen for the measurements was approximately 50 (49.85 based on calculations) degrees sun elevation angle that mimics what the Sun's elevation angle would be during the summer at midday in the study area of Vantaa, Finland. The illumination zenith angle was set at 40-degrees because it corresponds to conditions that are typically present in satellite imagery taken of the established study area. In addition, there are previous

studies of woody tree structures which had similar conditions (even though measured outdoors in natural lighting) [56]. The 40-degree zenith angle for the lamp incident on the sample was acquired when the sample surface height was at 9 cm, and it is the same height at which the axis of rotation of the system was set at (Fig. 11). This means that each sample surface and white reference target surface measured had to be confirmed to be at that height. So, if the sample or white reference panel was less than 9 cm in height, it was raised with 2 mm thick rectangular steel plates until 9 cm height was acquired. Measurement distance was set to 50 cm (Fig. 11). The 50 cm measurement distance allowed the 10-inch Spectralon white reference target to fit the entire field of view of the Specim IQ camera from this distance (FOV of 31 degrees covers a 27.7×27.7 cm area from nadir with the 50 cm measurement distance, and the 10-inch target is 25.4×25.4 cm). Noteworthy is, that the 50 cm measurement distance was a compromise between minimizing the illumination-view angle variation within the sample's surface and maximizing the number of pixels representing the sample (Fig. 11). In addition, the sample was always placed so that the "top"-side (direction of growth towards top of tree canopy) was towards the lamp (Fig. 11) and "bottom"-side (direction towards roots) away from lamp. "Top"-side and "bottom"-side will be used in this study to describe these two directions.

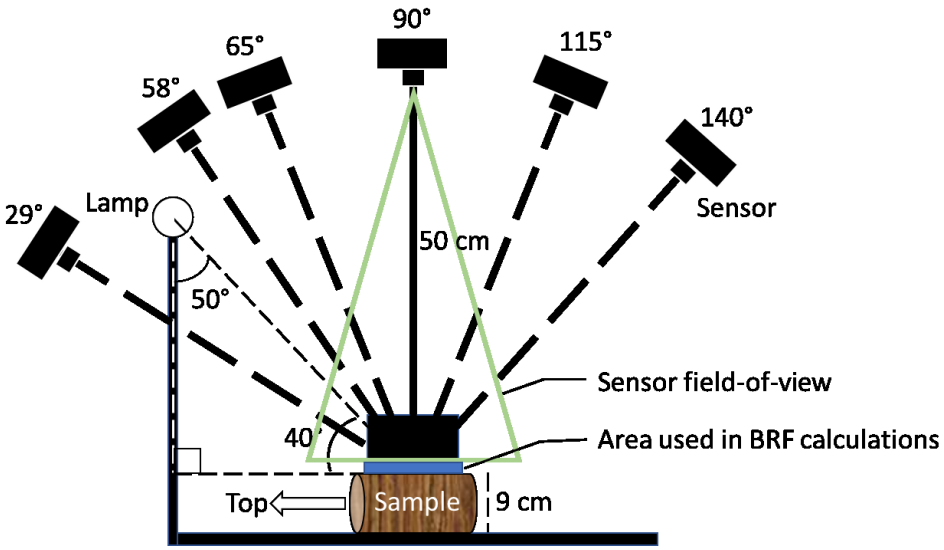

Figure 11. Measurement geometry with six different view angles along the principal plane (29, 58, 65, 90, 115 and 140 degrees relative to the table) and one fixed illumination angle. Measurement height from table set at 9 cm due to where the arm's axis of rotation is set. Measurement height between the axis and sensor is 50 cm. Green triangle represents the field-of-view of the sensor and the blue region depicts the masked area used in BRF calculations. Sample was always placed with "top"-side (canopy growth direction) towards lamp.

Six measurement angles were chosen for this study: 29, 58, 65, 90, 115 and 140 degrees relative to the table (Fig. 11). Due to the amount of time it would take to measure more angles, and the angular limitations of the system, the six angles were sufficient for this experiment. Angles 29 and 58 were the closest possible degrees near the hot spot, before the lamp obstructed the sensors view of the sample. Additionally, the 65° angle was selected in the backward-scattering side to get half the measurements from near the hot spot. As touched upon in theory and background, forest canopies have a strong hot spot effect in remote sensing and it is an interesting phenomenon to study whether similar relationship is

observable with just woody tree structures. The nadir view angle of 90 degrees is a commonly used view angle that is perpendicular to the target, and it has been used in previous studies as mentioned earlier [56]. The forward-scattering direction had two angles, 115 and 140 degrees. These two were selected to investigate the possible specular reflections that might occur directly from the sample causing more prominent BRF values in the forward-scattering direction.

3.5.2 Measurements of woody tree samples

As a reminder, BRF is the ratio of the reflected radiant flux from a given target surface to the reflected radiant flux from a perfectly diffuse standard surface (Lambertian) under identical view and illumination geometry. This equals to having a spectrum of a sample that is then normalized with the spectrum of a Spectralon® white reference standard. For this study it means that for each stem sample, a hyperspectral image of the sample was collected with the Specim IQ, and a hyperspectral image of the white reference was collected as well, for each of the established 6 view angles. These pairs of images were then used to calculate BRF values.

In addition to the hyperspectral imaging from multiple angles, the stem samples were photographed from the established view-illumination geometry identical to the hyperspectral images using the Nikon D5000. Finally, every sample's height, width, length, species, tree id, collected height and major compass direction (south-side or north-side) were recorded together with the accompanying file names.

3.5.3 Measurement protocol

The Specim IQ is very user-friendly and straightforward to use. The measurement process for the Specim IQ in its Default Recording Mode is divided into 5 distinct steps. The camera is also able to provide an Application Mode (processing model developed by Specim IQ Studio software) and an Automatic Screening Mode (one-class classifier) but these were not used in this study.

The first step is to direct the camera to the illuminated target using its viewfinder camera (RGB camera that is identical in viewing direction but with a small vertical offset to the hyperspectral camera). In this case, it means that with the goniometer, the camera was set to the correct angle and it was checked that the sample was within the field of view.

The second step is to choose the white reference that the camera will be using for reflectance calculations. There are three options: define a custom white reference by imaging a white reference before imaging the target, image white reference panel aside the target (simultaneous) or use pre-defined white reference installed in the camera (general halogen spectrum). Even though the custom data processing chain in this study does not require this step, the first white reference option was used in the measurement process to get quick validation reflectance values further in the measurement process of the camera. The area scan over the white reference is performed so that 100 random spectra are averaged and used for calculating the reflectance values. The size of the white reference area can be changed with a slider by the user. Using the slider increases or decreases the area based on a pixel intensity threshold. In this study, a 1.25-inch Spectralon® white reference target was used as custom white reference, and the surface area of the target was selected for the reflectance transformations.

The third step after defining the white reference, is to adjust the camera's integration time and focus for the target. The integration time can be set between the range of 1 to 500 ms. The camera proposes a preset value and the "optimal" range for the target, but a manual adjustment is possible. Focusing the camera is done manually. In addition to focusing the

system, the offset between the RGB camera and the hyperspectral camera can be adjusted manually if the provided automatic calibration fails. The automatic calibration is based on edge detection. The vertical parallax adjustment is needed if the user wishes to overlay the RGB and hyperspectral camera images. In this study, the integration times and focusing of the camera were set manually. In addition, if the automatic calibration did not succeed, it was adjusted manually.

The fourth step is to press capture and record the image data. The data acquisition records the dark current (sensor noise) of the sensor and then the full 512×512×204 image. After the data acquisition, the camera provides a data validation preview that shows an RGB image derived from the hyperspectral data and a pixel intensity histogram. The data validation preview allows the user to either discard or keep the data for further processing. Here is the option to only save the raw, uncorrected and unprocessed data. If the user decides to keep the data, the camera uses the white reference selection defined in step two to automatically transform the data to reflectance. Finally, after reflectance transformation the camera saves two sets of data cubes. The two separately saved data cubes in the data set are for the raw data (unprocessed) and the reflectance data (processed). This study used the raw data for further custom data processing.

The fifth and final step in the camera measurement process shows the calculated reflectance data in the camera user interface. Here it is possible to check the measured spectra and the spectral profiles, define a classification mask that is overlaid on an RGB image and add information on the recorded data. During the measurement protocol of this study (Table 3), the spectra of measured samples were checked during the final step to confirm data quality and recognize possible errors.

Noteworthy is that the white reference measurements done in the protocol for established 6 angles, using a Spectralon® white reference target, were conducted within every 90 minutes (Table 3). Therefore, the white reference measurements were not done for every sample, but rather within a set time limit. The 90-minute limit was selected for practical reasons, in order to limit the overall time used for the measurements. The stability of the light source was measured with an ASD FieldSpec 4 spectrometer, and the irradiance was found to be practically unchanged (±0.5–1.4%) during a one-hour monitoring period. In future studies it might be possible to reduce the frequency of white reference measurements even further. However, in this pilot campaign it was considered important to take white reference measurements at frequent intervals, to obtain a better understanding of the stability of the light source and the camera over long time periods.

To summarize, 720 hyperspectral images and 720 high-resolution RGB images were collected for the total 120 stem samples (one hyperspectral and one RGB image per angle per sample). The measurement protocol for both hyperspectral and high-resolution RGB images can be seen in Table 3.

Table 3. Measurement protocol used in this study for stem samples. The first column describes the view angle set for the sensor, second column describes what the sensor sees, and the third column defines the frequency of each performed measurement.

View angle (degrees)	What is imaged?	Frequency
Measurements with Specim IQ		
90	1.25-inch Spectralon® white reference target	Every 90 minutes
29	10-inch Spectralon® white reference target	Every 90 minutes
58	10-inch Spectralon® white reference target	Every 90 minutes
65	10-inch Spectralon® white reference target	Every 90 minutes
90	10-inch Spectralon® white reference target	Every 90 minutes
115	10-inch Spectralon® white reference target	Every 90 minutes
140	10-inch Spectralon® white reference target	Every 90 minutes
29	Sample	Each sample
58	Sample	Each sample
65	Sample	Each sample
90	Sample	Each sample
115	Sample	Each sample
140	Sample	Each sample
Measurements with Nikon D5000		
29	Sample	Each sample
58	Sample	Each sample
65	Sample	Each sample
90	Sample	Each sample
115	Sample	Each sample
140	Sample	Each sample

3.6 Data processing chain

To calculate BRF quantities for each pixel in the sample image, a data processing chain using Python programming language was developed for the raw data produced by the sensor. The reason a processing chain was developed for this study, is that it allows to calculate and extract accurate pixel specific reflectance information that is invariant to uneven spatial distribution of incident irradiance from the lamp (Fig. 5).

The raw data of an image acquired with the Specim IQ consists of measured digital numbers for each pixel and the dark current data associated for each raw image. The dark current data is noise produced by the electronics within the sensor and is a quantity that needs to be removed from the captured pixel digital numbers in the image. Then in addition to taking the BRF of the measured white reference target to consideration in the equation, it is often that the integration times used by the sensor are different between the sample and the white reference. This needs to be taken into consideration when calculating BRF quantities to make them accurate and comparable. These considerations were applied to the following equation, which was used to calculate the ratio between the white reference and sample images:

$$\mathrm{BRF} = \frac{\mathrm{DN}_{\mathrm{sample}(t1)} - \mathrm{DC}_{\mathrm{sample}(t1)}}{\mathrm{DN}_{\mathrm{white\_reference}(t2)} - \mathrm{DC}_{\mathrm{white\_reference}(t2)}} \times \frac{t2}{t1} \times \mathrm{BRF}_{\mathrm{white\_reference}} \quad (9)$$

where,

DN_{sample} is the digital number of pixels in the sample image,
DC_{sample} is the dark current values for pixels in the sample image,
$DN_{white\_reference}$ is the digital number of pixels in the white reference image,
$DC_{white\_reference}$ is the dark current values for pixels in the white reference image,
$BRF_{white\_reference}$ is the BRF quantities for the white reference target obtainable from the calibration file provided by the manufacturer. If not calibrated, 0.99 could be used to estimate the BRF of a Lambertian surface,
$t1$ is the integration time in milliseconds [ms] used to capture the sample,
$t2$ is the integration time in milliseconds [ms] used capture the white reference.

Ultimately, this established data processing chain differs from the Specim IQ's automatic reflectance transformation with a defined white reference area in one distinct way. With this data processing chain the normalization with the white reference is pixel specific, not a mean value acquired over 100 random pixels chosen from the area selected by the user. This pixel-wise processing attempts to correct for the spatial variation of lamp irradiance. In addition, another difference that is at least specific to this study, is that a correction was made with the BRF quantities for the white reference target. So, the algorithm used in Specim IQ is simplified to:

$$\mathrm{BRF} = \frac{\mathrm{DN}_{\mathrm{sample}(t1)} - \mathrm{DC}_{\mathrm{sample}(t1)}}{\mathrm{DN}_{\mathrm{white\_reference\_mean}(t2)} - \mathrm{DC}_{\mathrm{white\_reference\_mean}(t2)}} \times \frac{t2}{t1} \qquad (10)$$

In the results and discussion, where different algorithms are compared (Section 4.1), Equation 9 is referred to as "pixel-by-pixel algorithm", and Equation 10 is referred to as "Specim IQ's internal algorithm". The rest of the results were obtained using Equation 9.

Next, the data processing chain included creating masks that select pixels that represent the measured samples. Each of the six measured angles were attached with their own rectangular mask, each slightly different in size (varying from approximately 8 500 to 19 500 pixels) due to the viewed area changing with view angle. The masks for each angle were made to fit the smallest stem sample out of the 120. This was done so that the 120 samples could be masked automatically, rather than manually creating masks for each sample and each angle. The selected pixel locations by the masks were then used to calculate the BRF values with the established equations with collected pairs of sample and white reference images. The large number of pixels, now with accompanying reflectance quantities, could then be used further to describe spectral characteristics of the collected samples. These include the between-species, spatial and angular variations in the measured samples.

4 Results and discussion

4.1 Evaluation of the data processing chain and performance of the hyperspectral camera

To validate the designed data processing chain, an experiment was made using the Spectralon® reflectance standards. This was conducted to verify that the integration time correction and the pixel-by-pixel calculations work, and that they could be used in the actual measurement campaign. The results from this experiment were then compared with a set of processed reflectance values calculated and processed with the Specim IQ's internal algorithm, and extracted from the reflectance data cube, which is a standard output from the camera.

The experiment was done so that each of the five 1.25-inch standards (2, 10, 20, 50 and 99 percent in reflectance) were imaged from 90°, placed at the same position on the base table with the same established illumination-angle. Imaging was done in two different ways: first using same integration time for all standards and second, using different integration times (longest possible for each standard before over exposure at any pixel level). Each image was then identically masked to include same pixel locations which were used in the established processing chains. The masked 99 percent standard was used as the normalizing white reference. For both measurements, the established pixel-by-pixel algorithm (Eq. 9) from Section 3.6 was implemented.

The results indicated that both the integration time correction worked as intended (no differences in the two spectra), and that the pixel-by-pixel calculation provided accurate and pixel specific reflectance information (Fig. 12). The justification for the need of a pixel-by-pixel data processing chain was revealed when the results showed notably smaller standard deviation (Table 4) in comparison to the Specim IQ's internal algorithm (Eq. 10 from Section 3.6). For example, for the Spectralon standard with 50 percent reflectance, the standard deviation was 0.0275 with the Specim IQ's internal algorithm and in comparison, it had 0.0075 standard deviation with pixel-by-pixel algorithm (Fig. 12, Table 4). The larger standard deviation for the Specim IQ's internal algorithm was most likely due to the uneven spatial distribution of incident irradiance from the single source of illumination, and this could already be seen on a small 1.25-inch diameter circular surface area. This is significant, as larger samples (e.g. the 20 cm stem samples) would have even greater differences. The "top"-side of the sample was significantly closer to the lamp (as illustrated in Fig. 11), which produced higher digital numbers due to the uneven distribution of irradiance. More specifically, the larger standard deviation is supported most likely due to the way the white reference was calculated and used for normalizing in the Specim IQ's internal algorithm. As a reminder, the internal algorithm takes 100 random white reference values across a user defined surface area and averages them. Regardless of the processing method in this experiment, the Specim IQ gave comparable and accurate spectra for the measured standards in this non-repetitive experiment.

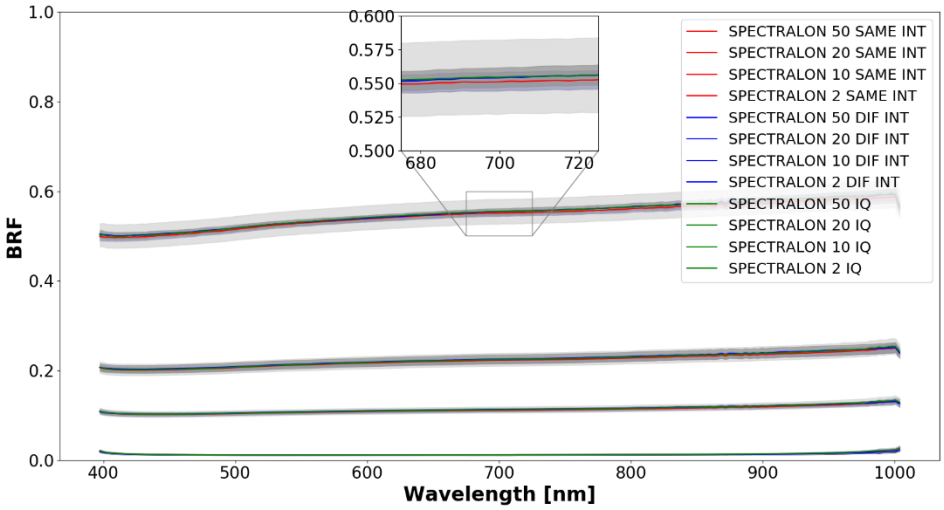

Figure 12. Spectralon reflectance standards (nominal reflectance values of 0.02, 0.10, 0.20, and 0.50) were measured with Specim IQ, and different processing chains were compared and evaluated. Red lines show standards measured with same integration times and processed with pixel-by-pixel algorithm (Eq. 9), blue lines show standards measured with different integration times and processed with pixel-by-pixel algorithm (Eq. 9), and green lines are results gathered from sensor processed reflectance values with same integration times (Eq. 10). The internal algorithm in Specim IQ produces results with noticeably higher standard deviations most likely because of uneven distribution of incoming irradiance (shown in the largest light grey area within the zoomed in figure).

Table 4. Mean, standard deviation and coefficient variation (averaged over all measured wavelengths) listed for each reflectance standard (nominal reflectance values of 0.02, 0.10, 0.20 and 0.50 percent) which were calculated after using Specim IQ's internal algorithm (Eq. 10) and pixel-by-pixel algorithm (Eq. 9). Calibration data of each standard shown for comparison of mean values.

	0.02	**0.10**	**0.20**	**0.50**
			Mean	
Calibration certificate	0.0088	0.1098	0.2099	0.5353
Specim IQ internal	0.0129	0.1128	0.2233	0.5495
Pixel-by-pixel (same integration times)	0.0127	0.1117	0.2216	0.5458
Pixel-by-pixel (varying integration times)	0.0123	0.1131	0.2242	0.5494
			Standard deviation	
Specim IQ internal	0.0017	0.0070	0.0142	0.0275
Pixel-by-pixel (same integration times)	0.0014	0.0040	0.0062	0.0075
Pixel-by-pixel (varying integration times)	0.0010	0.0030	0.0099	0.0078
			Coefficient of variation	
Specim IQ internal	12.88 %	6.19 %	6.35 %	5.01 %
Pixel-by-pixel (same integration times)	11.32 %	3.54 %	2.82 %	1.38 %
Pixel-by-pixel (varying integration times)	8.35 %	2.65 %	4.40 %	1.42 %

Even though the non-repetitive experiments conducted in the beginning of this study showed flat and stable results, the sensor showed some peculiar behavior when same targets were measured in short intervals and in high repetitive manner across multiple days. Systematic offset and instability in measured digital numbers were found in the beginning (approximately 400–415 nm) and end (approximately 925–1000 nm) of the measured

wavelength range. This was a source of error for the BRF calculations within those wavelengths. A previous evaluation study on Specim IQ conducted by Behmann et al. 2018 [12], also reported some limitations for the camera. For the bands between 400 and 415 nm, limitations were found for some materials and for bands between 925 and 1000 nm, limitations were observable when measuring in direct sunlight (which could be comparable to the conditions present in this study) [12]. It has also been mentioned that it is recommended to use some other sensor, if the measurement setup requires high level of repetitions, but no further explanations were given for this [12]. However, due to these found sources of error, the measured results that will be shown later, have been clipped to hold wavelengths between 415 and 925 nm. The limitations and probable causes for these errors in the sensor, in concordance to the earlier evaluation study, could be due to the materials measured, source of illumination, and short integration times (and the combined interaction with the sensor itself). Finally, the results and information gained from evaluating the data processing chain with known reflectance standards, gave insight and validation for the theory developed and allowed this study to continue forward with the multi-angular measurement of stem samples.

To further evaluate the data processing chain after the measurement campaign was completed, the pixel-by-pixel calculation process was investigated with the measured stem samples. This was done to see whether there were systematic trends visible along the length of the sample even after undergoing the data processing chain. Results indicated that there were no strong systematic trends visible and this suggested that the developed and designed data processing chain was successful.

4.2 Between-species variation

The two coniferous species, spruce and pine, had similar VIS reflectance that was distinctly lower than the VIS reflectance of birch (Fig. 13). Birch also displayed highest standard deviation among measured spectra with spruce having the lowest standard deviation of all three species (Fig. 13). When observing closer at each species and sample trees, spruce BRF varied between 0.07–0.52 for “Spruce 1”, and between 0.07–0.54 for “Spruce 2” (Fig. 14A). Pine BRF varied between 0.08–0.60 for “Pine 1” and between 0.07–0.62 for “Pine 2” (Fig. 14B). Birch BRF varied in a more limited range between 0.20–0.57 for “Birch 1” and between 0.21–0.53 for “Birch 2” (Fig. 14C). Birch reflectance from VIS to NIR was soil-like and increased monotonously (Fig. 13, Fig. 14C). Birch was also quite flat in spectra and did not show typical vegetation characteristics (e.g. strong absorption at red and blue wavelengths, sharp rise at red edge) strongly [14]. High variations between samples were present for birch, which could also be seen as higher standard deviation as mentioned earlier (Fig. 13). In comparison, both spruce and pine displayed some magnitude of red-edge effect that is typical for green vegetation (Fig. 13) [14]. This could be explained with the undetermined visible green vegetation (mosses, lichens) that grew on top of the bark, especially on spruce (Fig. 15A). The green vegetation that is not specifically tied to the tree species itself (e.g. external lichen or mosses growing on the bark), was not as strong with the pine samples, but the pine displayed greenish characteristics under the top most bark layer when going higher up on the stem (Fig. 15B). In general, the bark was much brighter for birch (nearly white in large areas of the samples) with very dark regions as contrast (Fig. 16A–B). The largest between-species differences within the measured VIS-NIR wavelength range could be seen in NIR, with emphasis around the red-edge region (Fig. 13, 14). Finally, spatial details could be investigated through both RGB representations of hyperspectral images and the separate RGB images (Fig. 16A versus 16B, Fig. 16C versus 16D).

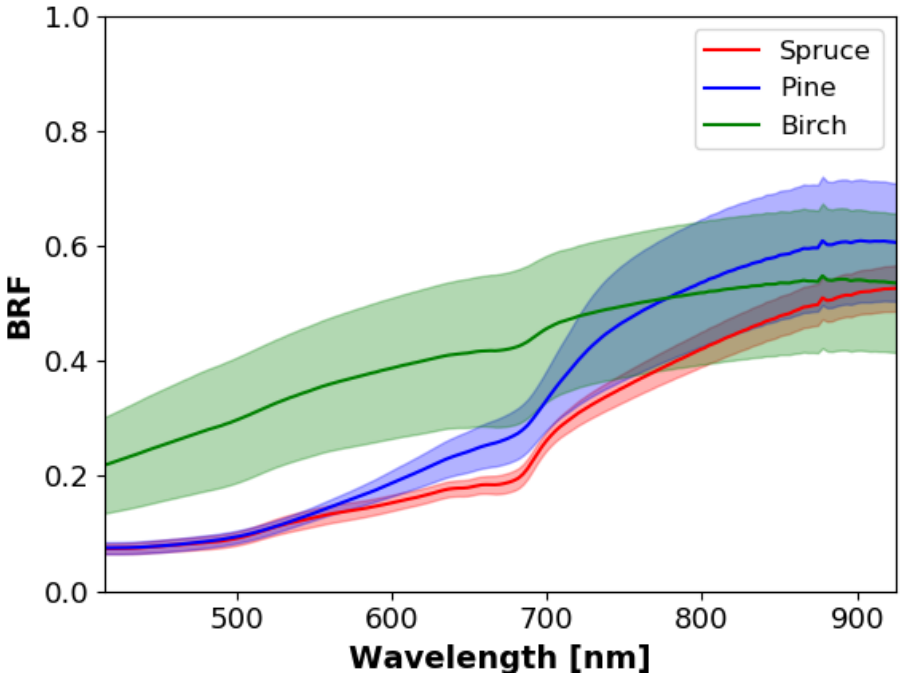

Figure 13. Mean and standard deviation for spruce, pine and birch spectra. Standard deviation was calculated between the mean spectra of samples for each species.

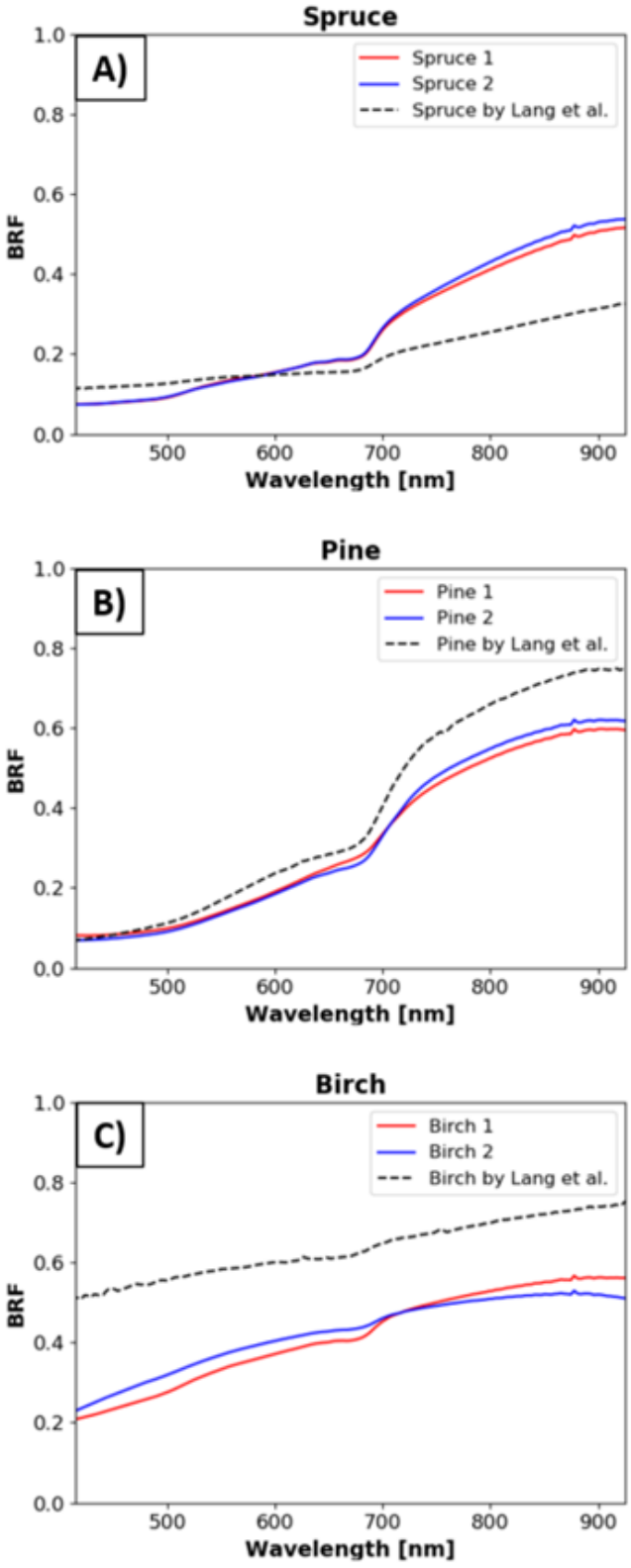

Figure 14. Mean reflectance for each sample tree collected from 90° view angle (i.e. perpendicular to the sample surface). Subfigures A, B and C illustrate the mean reflectance of measured spruce, pine and birch trees respectively (blue and red lines separate sampled trees per species). Each species-specific plot has been appended with the mean reflectance measured in an earlier study by Lang et al. (2002) for comparison (dashed black line). The data by Lang et al. (2002) is available from [56].

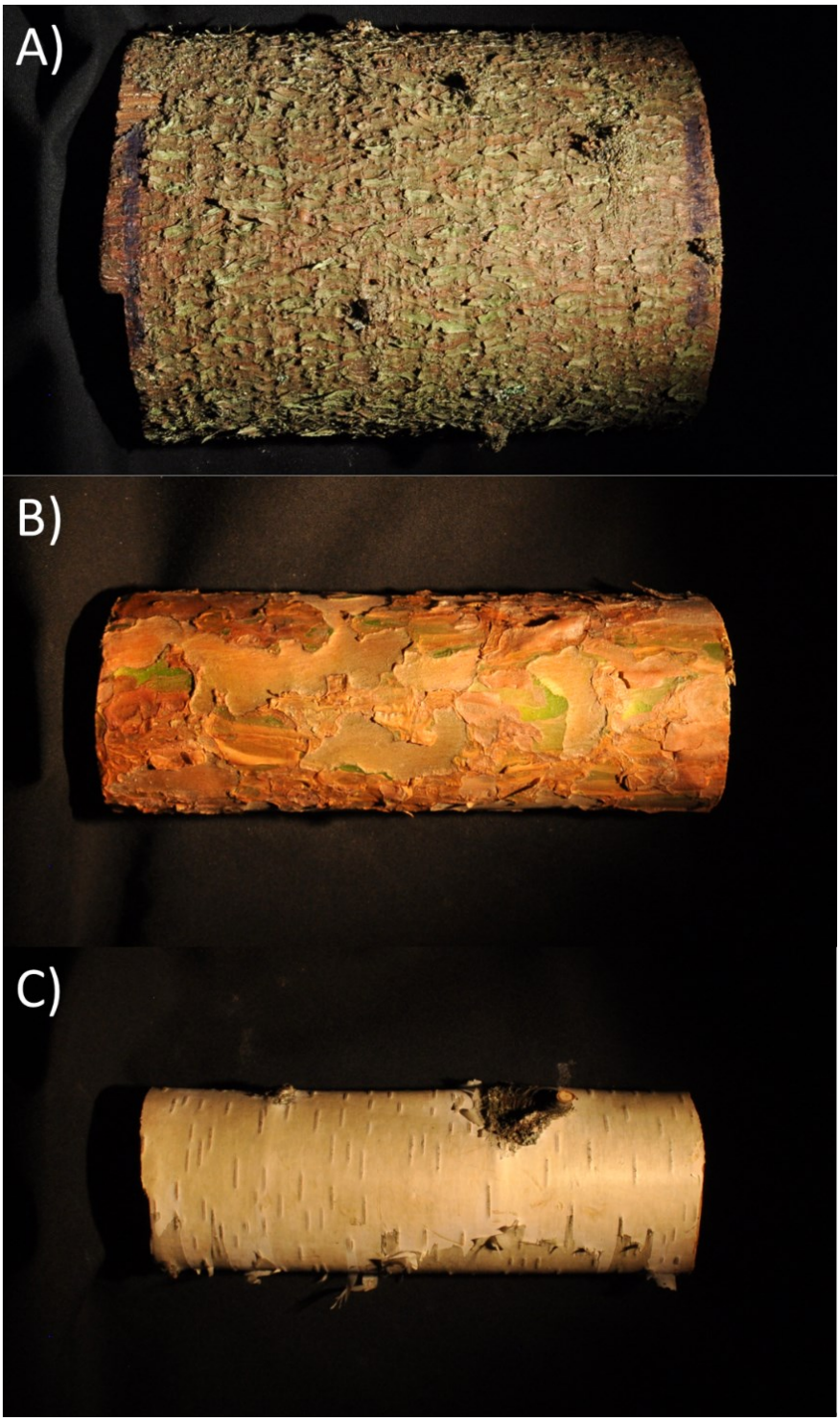

Figure 15. RGB images of A) spruce sample from 5 m height on the north-side displaying green vegetation characteristics among the woody tree structures, B) pine sample from 9 m height on the north-side showing greenish bark characteristics among the typical reddish-yellowish tones, and C) birch sample from 9 m height south-side with large smooth and bright sample area.

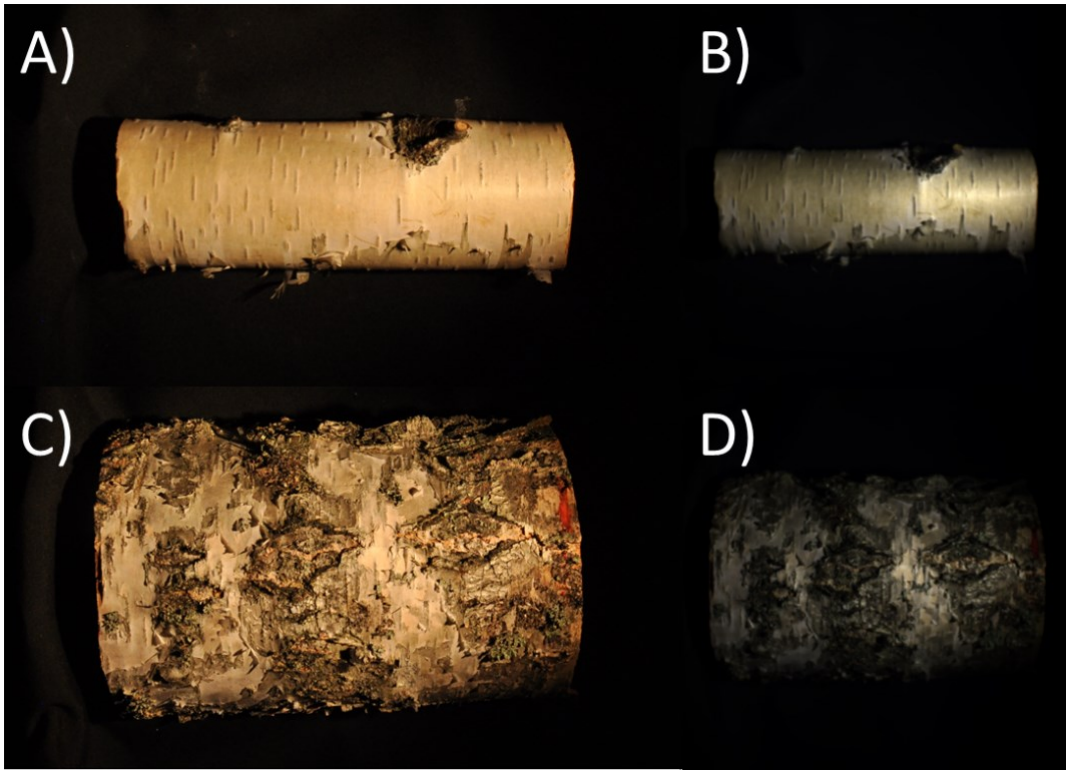

Figure 16. Example of large differences in birch samples obtained with Nikon D5000 (A, C) and Specim IQ (B, D). Upper row: A birch sample with smooth and bright areas. Lower row: A birch sample with large dark areas and uneven surfaces.

In addition to the spectra measured in this study, the mean spectra measured in a previous study by Lang et al. (2002) (publicly available open data, collected from [56]) was plotted for comparison (Fig. 14). They conducted a series of measurements of tree trunk bark for spruce, pine and birch (same species as in this study). The reflectance spectra measurements were conducted in June-July of 2001, in the forests of Järvselja and Konguta regions in southeast of Estonia and in the Siggefora-Kättböle and Stockholm regions in Sweden [56]. The spectra were collected with a GER-2600 spectrometer that operates in the wavelength range of 400–2460 nm. Measurement height for the bark spectra was approximately 1.8 m and measurements were made preferably on sunny days. They measured three bark samples of birch, two bark samples of spruce, and six bark samples of pine. All spruce and birch samples measured were of growing trees, but for pine they measured 5 samples of pine logs (either upper or lower half of tree trunk) and one sample of growing pine tree (at 1.8 m from ground). Noteworthy is that the similarities and differences between these two measurement campaigns affect the comparability and can explain why results differ. Perhaps the most notable aspect was that these two studies were difficult to compare quantitatively due to the varying sampling schemes, e.g. different number of sampled trees per species, measurements made outdoors in natural sunlight (varying sun elevation angles), and number of measurements (samples) per tree.

However, when comparing to the results reported by Lang et al. (2002), the general shapes of mean spectra for the different species are similar to the mean spectra collected in this study (Fig. 14). As mentioned, they measured fewer samples in general which affected the differences in mean reflectance. Pine was very close to what this study recorded in shape and in magnitude of BRF quantities (Fig. 14B). Lang et al. (2002) also recorded pine bark being greenish or greenish-yellowish in upper half of the tree trunk (similar findings were

found in this study). Pine had some typical green vegetation characteristics when moving up the stem (typically quite grey or brownish in color near the lower half). The mean birch spectra reported by Lang et al. (2002) differed in magnitude and was distinctly higher in reflectance, even though the shape of spectra was much like the spectra measured in this study (Fig. 14C). This was most likely due to having a very bright sample in the three measured samples. When inspecting the spectra measured in this study, there were samples with similarly higher spectra and shape, but when averaging all samples, the mean spectra became much lower. Spruce perhaps had the most differing spectra between these two studies, especially when looking at the NIR region (Fig. 14A). VIS region for spruce had similarities and was monotonously low and flat in shape, but the same trend looks to continue for measurements made by Lang et al. (2002). After inspecting photographs of spruce samples measured by Lang et al. (2002), it seemed that the samples measured in this study had more lichen and other green material on top of the spruce bark, which possibly explains why the NIR reflectance was much higher.

The clear differences in between-species variation when inspecting the mean spectra and standard deviations (Fig. 13) could be explained by the typical tree structure of each species. As spruce displayed the lowest standard deviation from the three species, it was likely due to the very similar composition of samples. The spruce samples, from both sampled spruce trees, displayed very similar bark surface throughout. Pine which had slightly higher standard deviation (especially at NIR), had clear changes in samples (visible changes in bark when comparing lower and upper half of the tree trunk). However, these changes in samples were not as strong as with birch, that had large differences present between samples (Fig. 16A, 16C).

In addition to similarities found with the study conducted by Lang et al. (2002), encouraging support was found with other studies that had made bark measurements of same species or genus. Previous studies have concluded that bark reflectance is highly variable between species (even between conifer species), but the shapes of spectra can be described to be similar or same [9, 57]. After comparison was made with studies [9, 56, 57, 58], the general shapes of spectra measured were found to be similar in this study as well.

4.3 Angular variation

The angular variation within-species was investigated by calculating tree specific mean reflectance for all measured six angles (29, 58, 65, 90, 115 and 140 degrees) along the principal plane. Each mean reflectance holds a total of 20 samples.

Interestingly, differences were present between-species and not much between individuals of same species. Even though each sampled tree for all three species were unique, the angular variations and spectra for each angle within-species were nearly identical (Fig. 17). The most interesting difference observable, in contrast to some conclusions made in earlier between-species section, was how the pine and birch trees behaved similarly (Fig. 17 C–F) while the spruce tree samples behaved differently to the two other species (Fig. 17 A–B). The study revealed that both pine and birch had noticeably stronger reflectance in the forward-scattering direction (115° and 140° view angle) compared to backward-scattering directions. However, spruce showed strong reflectance in the backward-scattering direction (especially for the 29° view angle), revealing a hot spot effect. However, statistics revealed that according to mean percentage differences, spruce also displays stronger values from forward-scattering direction of 140° view angle (having both hot spot and specular effects present) (Table 5). After closer inspection, the 140° view angle had higher BRF in VIS, but marginally lower BRF in NIR when compared to the 90° view angle.

When comparing to the spectra collected from 90° view angle, the two pine trees had 24 % higher BRF at 115° view angle, and 77 % higher BRF at 140° view angle. Birch had approximately 13 % higher BRF at 115° and 32 % higher BRF at 140° when comparing to the 90° view angle spectra. Spruce which showed a hot-spot effect, had a 31 % higher BRF on average when comparing the near-hot spot angle 29° to the 90° view angle.

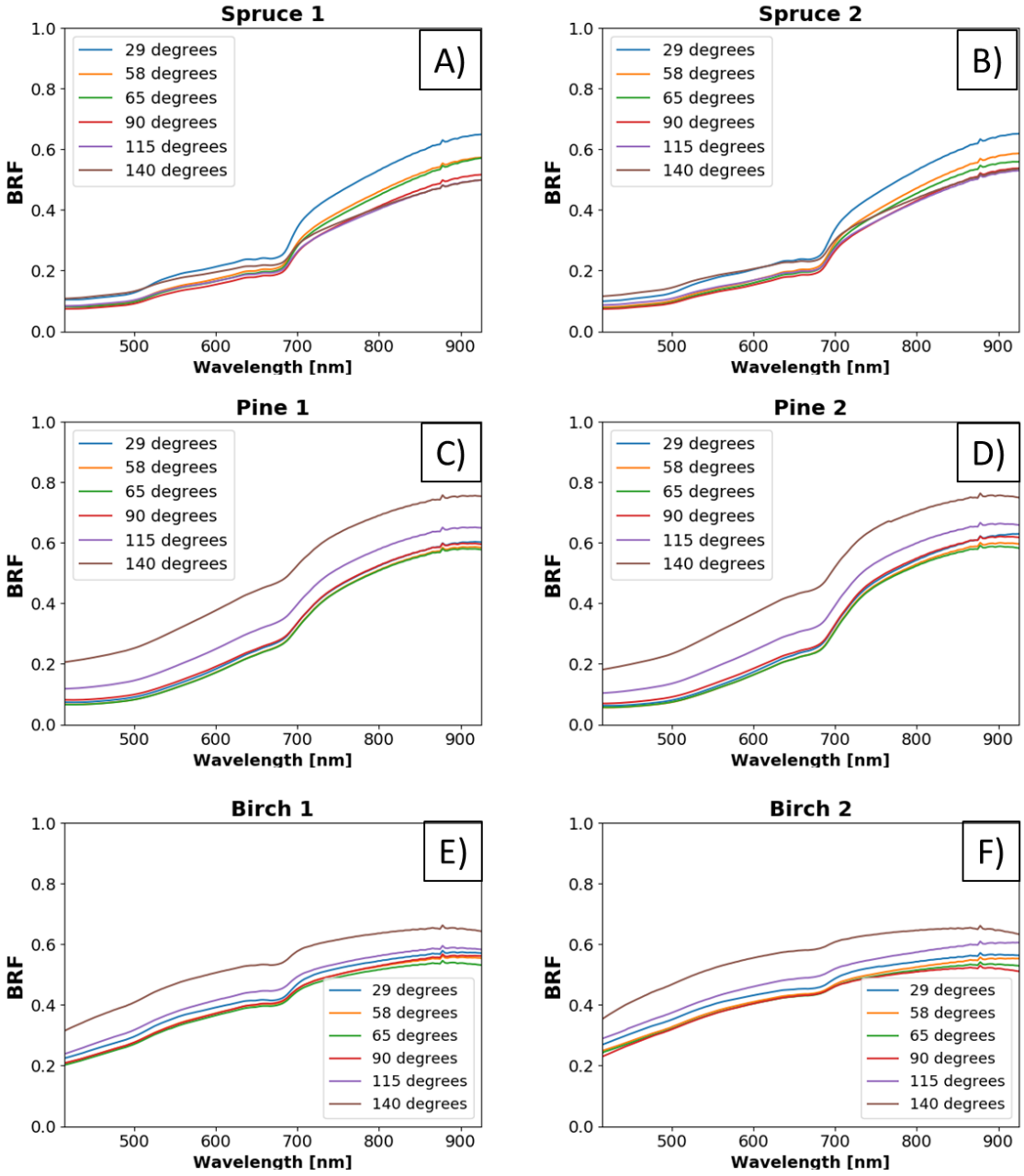

Figure 17. Angular variation of each measured sample tree. Each plot (A, B, C, D, E, F) shows the mean reflectance for each measured angle (29, 58, 65, 90, 115 and 140 degrees) of each tree (20 samples per mean reflectance). Spruce (A, B) shows a hot spot effect for the backward-scattering angle of 29°. Pine (C, D) and birch (E, F) behave similarly to each other with increased reflectance in the forward-scattering direction (angles 115° and 140°) having stronger reflectance.

Table 5. Relative values of BRF at different view angles when compared to 90° view angle (perpendicular to sample).

Tree ID	29°	58°	65°	90°	115°	140°
Spruce 1	133.29 %	111.55 %	108.75 %	100 %	103.55 %	116.85 %
Spruce 2	128.46 %	109.30 %	104.22 %	100 %	106.25 %	123.13 %
Pine 1	97.27 %	92.20 %	91.38 %	100 %	124.17 %	177.65 %
Pine 2	96.54 %	90.75 %	89.97 %	100 %	124.30 %	176.78 %
Birch 1	104.07 %	99.46 %	96.74 %	100 %	108.93 %	129.67 %
Birch 2	109.42 %	104.93 %	102.05 %	100 %	117.31 %	134.33 %

The strong reflectance in forward-scattering direction for pine and birch suggested specular reflections and this was supported by the structure of the bark. Both pine and birch presented much smoother surfaces than spruce, especially when going higher up on the stem, that allowed for specular reflections to occur (Fig. 18). The spectra showed this to be true, but also as a practical observation, the integration times used for the forward-scattering angles had to be made relatively much shorter to avoid over-exposure. Similarly, the reason why spruce behaved differently in multi-angular measurements, was most likely due to the structural characteristics of the spruce bark. The bark for both spruce tree samples had noticeably more coarse and uneven surface properties. After inspecting the high-resolution RGB images (Fig. 18), it looked as if the bark structures were aligned so that when imaged from the forward-scattering side, the structures created small shadows throughout the sample (Fig. 18). These small shadows add up and possibly lower the overall reflectance in such a way, that spruce had a more prominent reflectance near the hot spot, rather than in the forward-scattering direction like pine and birch. This did not however explain why spruce showed higher reflectance in VIS, but not at NIR when viewed from 140° view angle. This suggests that spruce had a more complex angular behavior present.

At the time of this study, similar publications that research the angular variation of woody tree structure spectra were not found. The results found in this study are novel.

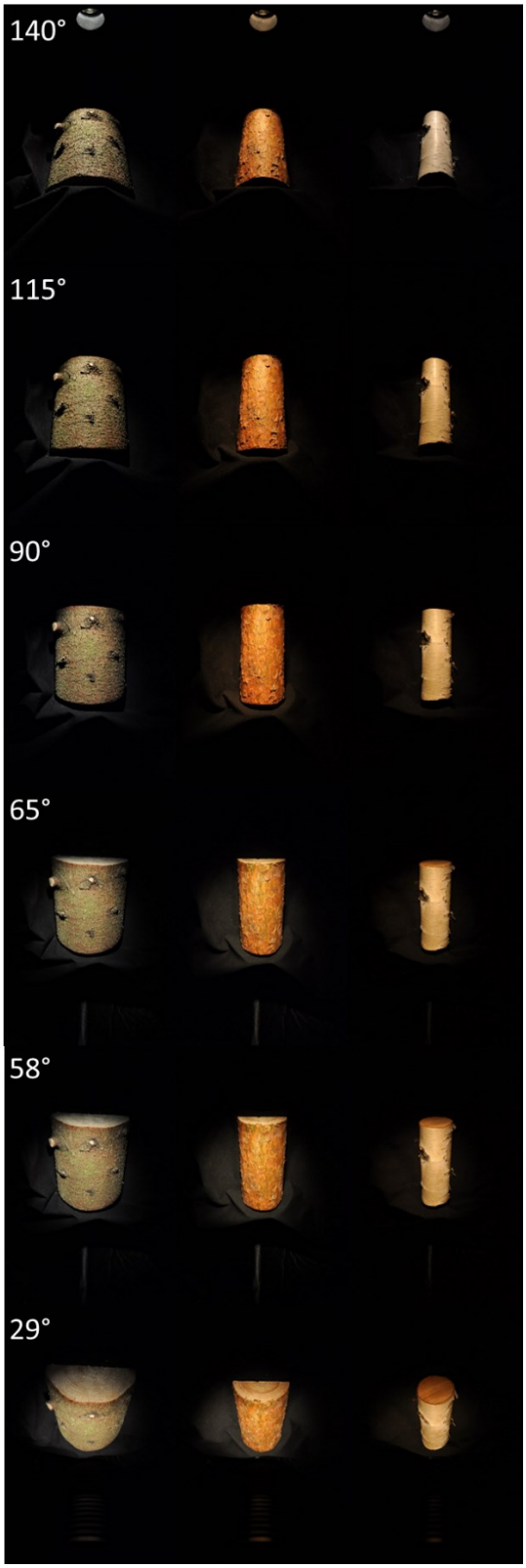

Figure 18. High-resolution RGB images that were used to support the data analysis of angular variation of reflectance. Figure shows one example per tree species (from left to right columns: spruce, pine and birch) imaged from all six angles (29, 58, 65, 90, 115 and 140 degrees). Birch and pine show brighter surface at 115 and 140 degrees, while spruce is brighter at near-hot spot (29 degrees) with extending shadows at forward-scattering angles. Direction of illumination is from up to down (lamp visible on very top).

4.4 Spatial variation

Spatial variation of reflectance occurring at different heights and different sides of a tree (southward and northward facing sides of the stem) was investigated for few specific wavelengths measured perpendicular to the sample surface (90° view angle). More wavelengths were looked at, but this study will report the findings on blue (492.97 nm), green (560.3 nm), red (663.81 nm) and NIR (865.5 nm) wavelengths. These chosen wavelengths or bands are close to what are used as central wavelengths for the Sentinel-2A satellite bands, but these have not been processed with the sensor specific spectral response functions. This was to keep focus on the results obtainable with this custom built multi-angular measurement setup, even though the option to further process is available for the future. In addition, this study did not attempt to investigate how well the three different tree species were separable from Sentinel-2 satellite images. Hence, the channels were chosen for illustration purposes.

For the blue band, spruce (Fig. 19A) and pine (Fig. 19B) displayed very flat and small variation across the measured heights. They also showed very similar BRF quantities at this wavelength regardless of height, which was also observable in earlier results. More specifically, “Spruce 1” BRF varied between 0.080–0.097 on the north side and between 0.071–0.115 on the south side. “Spruce 2” BRF was very similar and varied between 0.060–0.089 for the north side and between 0.079–0.115 on the south side. “Pine 1” BRF varied between 0.077–0.103 for the north side and between 0.091–0.117 on the south side. “Pine 2” BRF was nearly identical and varied between 0.076–0.102 on the north side and between 0.074–0.106 on the south side. “Pine 1” displayed slightly higher BRF quantities for the blue band on the south-side from 4 to 10 m height than “Pine 1” north-side. On the other hand, birch had much more variation and there were observable differences between measurement directions as well (Fig. 19C). The BRF in relation to height varied between 0.197–0.313 for “Birch 1” north side and between 0.176–0.402 for south side. “Birch 2” BRF varied between 0.132–0.286 for the north side and between 0.282–0.558 for the south side. Interestingly, the spatial variation for birch shows higher BRF in blue band throughout the heights for the south-side, especially for “Birch 2”. “Birch 1” displayed higher reflectance in blue band on the south-side from 6 to 10 m height as well (Fig. 19C). The higher reflectance on south side for “Birch 2” could be perhaps due to the growing environment at the study site. “Birch 2” was located at a very open surrounding with a road on the southern side, perhaps allowing for greater incoming sunlight that might have affected the characteristics of the bark (surrounding visible in panorama photograph shown in Fig. 9D).

For the green band (Fig. 19D–F), the results showed nearly identical trends as with the earlier blue band (Fig. 19A–C). The difference in results is mostly that the magnitude of BRF is slightly higher with the green, which was expected as the spectra increased smoothly and were soil-like.

For the red band (Fig. 19G–I), spruce (Figure 19G) continued having very flat variation along the different heights, with a small change in the reflectance at 2 and 3 m heights for south-side “Spruce 1”. Birch (Fig. 19I) continued to show similar variation even for the red band. Interestingly, pine (Fig. 19H) displayed a pattern of having a small stable increase in BRF from 1 to 4 m height and then continuing with little to no change. The BRF increased for “Pine 1” on the north side 91 percent and 81 percent on the south side when going from 1 to 4 m height. For “Pine 2”, the increases were 59 and 35 percent. This could be due to the pine bark structure and color changing around that height range (visible to the human eye). High-resolution RGB images taken of samples were used to find possible explanations (Fig. 20).

The spatial variation in NIR (Fig. 19J–L) band showed that the reflectance of pine (Fig. 19K) grew from approximately 1 to 5 m height and then flattened after that. Similarly, to the results in red band (Fig. 19H), the BRF at NIR (Fig. 19K) for "Pine 1" increased 86 percent on the north side and 93 percent on the south side when going from 1 to 5 m height. "Pine 2" increased 76 percent on the north side and 73 percent on the south side when going from 1 to 5 m height. This behavior was visible for both sample trees and compass directions. In comparison to the other presented bands, spruce (Fig. 19J) displayed more changes between the compass directions measured for the NIR band, even though there did not seem to be any trend with tree height. Both "Spruce 1" and "Spruce 2" had slightly stronger reflectance on the north-side (Fig. 19J). Birch behaved the same way as it had with previous bands (Fig. 19L). Again, this is most likely due to the soil-like monotonously increasing spectra.

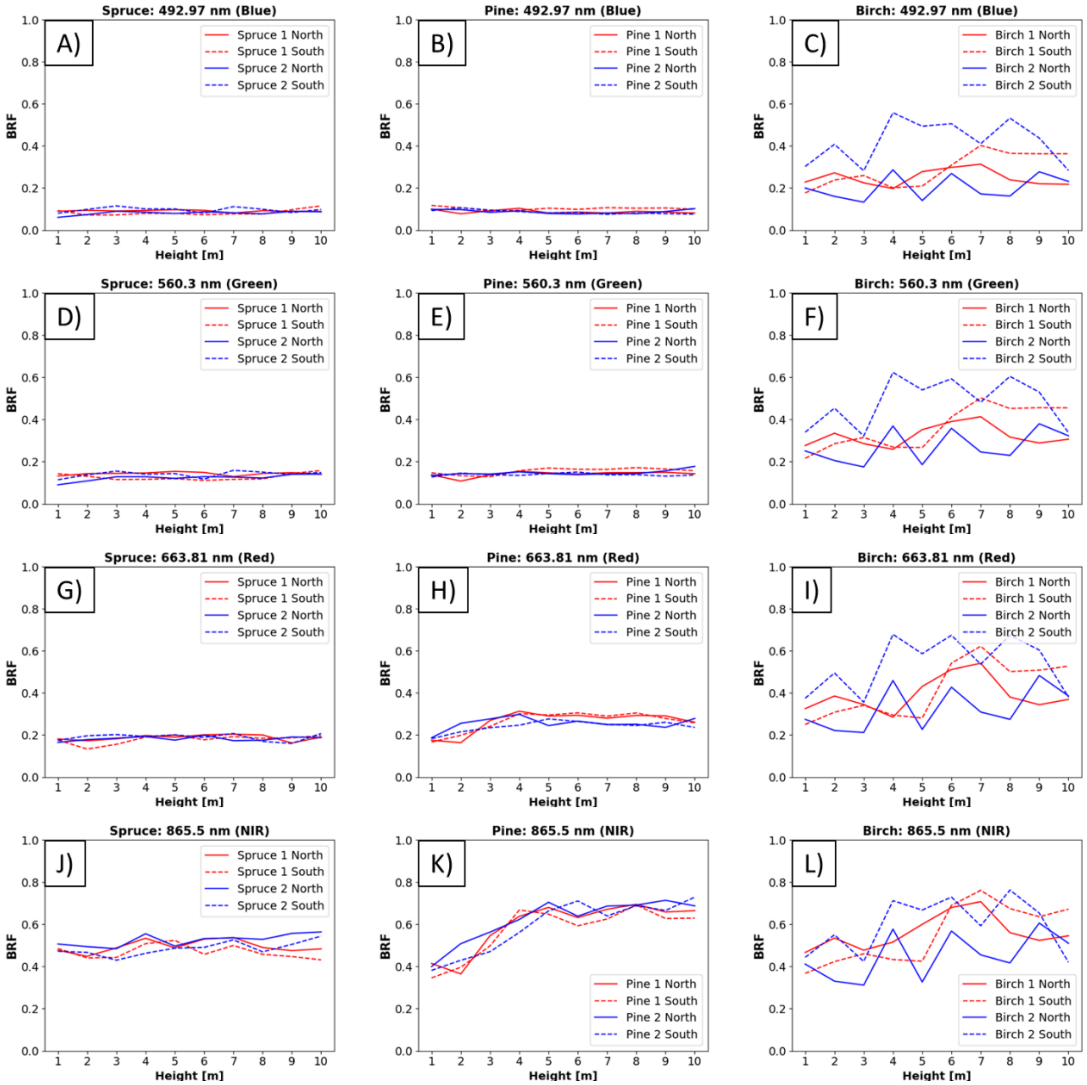

Figure 19. First row of plots shows spatial variation of reflectance at 492.97 nm (blue band) along tree height for spruce (A), pine (B) and birch (C). Second row shows spatial variation at 560.3 nm (green band) for spruce (D), pine (E) and birch (F). Third row shows spatial variation at 663.81 nm (red band) for spruce (G), pine (H) and birch (I). Last row shows spatial variation of reflectance at 865.5 nm (NIR band) for spruce (J), pine (K) and birch (L). For all plots A–L, red and blue colored lines represent the two different trees per species, where solid line is the north-side and dotted line is the south-side of the tree.

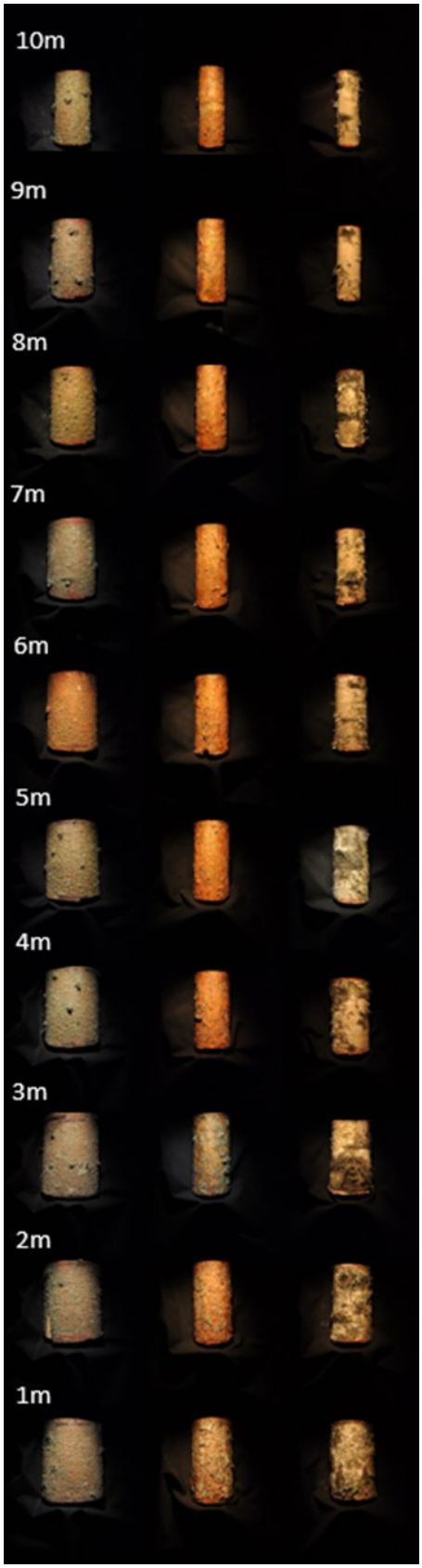

Figure 20. High-resolution RGB images gathered from each sampled height for one tree (left column shows spruce, middle pine and the right column displays birch), imaged from nadir.

At the time of writing this thesis, similar results that depict the spatial variation of spectra for spruce, pine, and birch at different heights and different sides of a tree (e.g. southward and northward facing sides of the stem) were not found. However, Lang et al. (2002) [56] did measure samples of pine logs from different heights, specified as upper or lower half of tree trunk. Further research could be made by acquiring more measurements from a wider sampling of trees.

4.5 Strengths and limitations of the collected dataset

4.5.1 Impact of sampling

The dataset that was collected during this pilot study is, to the knowledge of the author, one the largest spectral databases on woody tree structures to this date. In addition, the angular and spatial variation that was investigated for the three species has not been studied before to such extent. Even so, the trees that were selected for sampling were from forest stands that were of the same age and of close proximity to one another. This made the samples within same species very similar to each other, as they had grown in very similar surrounding conditions. Thus, the results found could perhaps be considered as site-specific. In addition to being sampled from nearly the same location, the number of sampled trees is a limiting factor in itself. The two sampled trees per species restricted the general conclusions that could be made, mostly for the spatial variations. On the other hand, the number of samples then collected for each species (40 samples) from the two trees, is what makes this dataset extensive in its own kind. The collection of a dataset that covers location, height and directionality for woody tree structures (i.e. bark) is tedious and difficult to do in large scales.

4.5.2 Impact of the measurement setup and data processing chain

The novel and experimental multi-angular measurement setup gives its own additions to sources of error or limiting factors. One of the weaknesses in this dataset is the restricted number of angles measured for each sample. As introduced and described in Section 2, the state-of-the-art multi-angular measurement facilities around the world can measure entire hemispheres for approximating the BRDF of surface materials, as opposed to the six measurement angles with this custom-built system. The six measurement angles were additionally limited to be taken from the principal plane only. However, the built system was one of the first multi-angular imaging systems and interpreting the substantial amounts of data collected for every measurement was challenging, making the limitations justified and needed. Furthermore, the six angles measured were enough to show the anisotropy of woody tree structures in reflectance. In addition to the multi-angular properties of the system, the artificial illumination most likely contributed to the errors found in measured spectra. Accommodating only one lamp of the chosen kind in the system was perhaps not enough, and a better illumination setup should be considered for the future. Possibilities for improving the illumination setup include using a more powerful lamp or trying a collimated light source. Such improvements could possibly result in more stable spectra for the full 400–1000 nm range of the sensor. The wavelength range of 400–1000 nm obtainable with the sensor is also limiting in itself, and a wider range could have provided more possibilities for species separation at SWIR region of the spectrum. Detailed limitations of the camera were presented in Section 4.1. The current option of manually rotating the measurement setup and adjusting to the correct view angle is slow and time consuming, which means that there is room to improve this by automating the system.

The designed data processing chain has an impact on the dataset as well. The main factor affecting the results was the chosen mask size for the samples. As described in Section

3, the mask sizes differ for each angle and only one size of mask was used per angle for each sample. This was done to automate the processing, but it is not optimal for results. The masks were created to accommodate the smallest sample found, but for larger samples, the amount of pixels used to calculate each spectra could have been increased if done manually. However, this again poses a problem when it comes to time consumption and the viability of doing so. It was a design choice that ultimately was a compromise.

In conclusion, the design and construction of the built system could be seen as an optimization problem. The goal was to maximize the amount of pixels representing the sample (i.e. having the sensor close enough to the sample), while attempting to minimize the sensor angle variation within the sample pixels (i.e. having the sensor far enough from the sample), and still allow the sensor to measure near the hot spot.

4.6 Implications for future use

The between- and within-species spectral variations discovered in this study are promising for developing more accurate forest reflectance models and for species classification applications. Forest reflectance models could be made more accurate through using more detailed input data of woody tree structures. Possibly the data and results that were already achieved in this thesis could be used for that purpose. The experimental nature of this pilot study could also be used as an inspiration for developing versatile spectral libraries of woody tree structures, which might reveal surprising impacts on the entire reflectance scene of forests when combined with simulations and modeling. In addition to developing and aiding the interpretation of models and remote sensing data, the results found in this study could be used for tree species classification purposes. Future interest could be directed at transitioning from typical airborne or spaceborne applications to ground-based applications within a forest. Forestry industry could possibly benefit from detailed knowledge of spectral properties of woody tree structures for automatic classification of trees. Automatic classification with onboard sensors (e.g. hyperspectral imaging sensors) for harvesters and other forestry equipment could be a game changer and a solution for the right applications in the future. Finally, the methods and materials presented in this study can give ideas for developing imaging multi-angular goniometer systems that can acquire even more information on various canopy elements.

5 Conclusions

This thesis has presented a novel and custom-built multi-angular measurement setup that was equipped with a state-of-the-art mobile hyperspectral camera (Specim IQ) that operates between the wavelength range of 400–1000 nm. The system was successful in facilitating the sensor and enabling measurements to be conducted along the principal plane and near the hot spot with high repetition needs. Using the measurement setup, this pilot study was able to collect multi-angular spectral data of woody tree structures from six different angles of the three most common boreal tree species found in Finland. The collected dataset is possibly one of the largest spectral datasets of boreal woody tree structures to this date. A total of 120 stem samples were collected from six trees, two for each species of Norway spruce, Scots pine and silver birch. Each of the samples were measured from six different angles, producing a dataset of 720 hyperspectral images. Furthermore, a pixel-by-pixel data processing chain, that is invariant to uneven spatial distribution of incident irradiance from the lamp, was used to reveal angular and spatial variations of reflectance in the measured samples. In addition to analyzing and reporting the found angular and spatial variations, this study looked at the between- and within-species variation of sampled trees.

Spruce and pine spectra behaved very similarly in VIS region of the spectrum but displayed larger differences between each other in the NIR region. In addition, spruce and pine showed relatively strong absorption at red and blue wavelengths and a rise near the red edge, which are also typical characteristics for green vegetation. Birch displayed generally higher BRF values across the spectra in comparison to pine and spruce. Furthermore, birch behaved soil-like and increased monotonously from VIS to NIR regions. Interestingly, the results showed surprisingly low variation within-species spectra. Comparison of same species spectra with previous studies concluded that the general shapes of spectra for different species were similar to each other. In concordance to the previous studies, the stem bark reflectance between species was found to be highly variable.

Investigating angular variation, in comparison to the measurement angle perpendicular to the sample surface, found that pine and birch behaved similarly by having distinctly stronger BRF in the forward-scattering angles than in the back-scattering angles. Surprisingly, spruce showed behavior that is more complex by having both hot spot and specular effects present. Nevertheless, the results suggest that the specular reflections and hot spot effects found for the three different species were present due to various structural properties of the bark.

Minor spatial variation of reflectance along the tree height and different sides of the stem (southward and northward facing sides of the stem) were found, but general reliable conclusions were difficult to make due to the low number of sampled trees. Further research could be made by acquiring more measurements from a wider sampling of trees. To summarize, four spectral bands (red, blue, green and NIR) were used to visualize the spatial variation for each of the three species. The results found that spruce showed no meaningful trends along the height of the tree for each of the four bands. This might be supported by the fact that spruce bark does not visibly change much along different heights of the stem. However, pine that does have a visible change in color of bark at different height of the stem, showed a clear increase in BRF for both trees from 1–4 m for the red band and from 1–5 m for the NIR band. Finally, birch showed similar trends for all four bands, most likely due to the soil-like nature of the spectra.

The results obtained in this study might be beneficial for future tasks such as tree species classification and the further development of forest reflectance models. The combination of detailed knowledge of spectral anisotropy in reflectance and extensive datasets of spectral properties of woody tree structures could be applied for automatic

classification of trees in the forestry industry. Automatic classification with onboard sensors (e.g. hyperspectral imaging sensors) for harvesters and other forestry equipment could be a game changer and a solution for the right applications in the future. Finally, the methods and materials presented in this study can give ideas for developing state-of-the-art imaging goniometer systems that can acquire even more information on various vegetation canopy elements than what was presented in this thesis.

References

[1] Tkachenko, N. (2006) 'Optical spectroscopy: methods and instrumentations', in *Optical Spectroscopy Methods and Instrumentations*. 1st ed. Elsevier Science. p. 322. ISBN 978–0–444–52126–2.

[2] Schaepman, M. E. (2008) 'Imaging Spectrometers', in *The SAGE Handbook of Remote Sensing*. SAGE Publications Ltd, London. p. 166-178. doi: 10.4135/9780857021052.n12.

[3] Danner, M. et al. (2015) 'Spectral Sampling with the ASD FieldSpec 4 –Theory, Measurement, Problems, Interception', *EnMAP Field Guides Technical Report, GFZ Data Services*. doi: 10.2312/enmap.2015.008

[4] Goetz, A. F. H. *et al.* (1985) 'Imaging spectrometry for earth remote sensing', *Science*. doi: 10.1126/science.228.4704.1147.

[5] Goetz, A. F. H. (2009) 'Three decades of hyperspectral remote sensing of the Earth: A personal view', *Remote Sensing of Environment*. doi: 10.1016/j.rse.2007.12.014.

[6] Homolová, L. *et al.* (2018) 'In situ data supporting remote sensing estimation of spruce forest parameters at the ecosystem station Bílý Kříž', *Beskydy*. doi: 10.11118/beskyd201710010075.

[7] Heiskanen, J. *et al.* (2013) 'Sensitivity of narrowband vegetation indices to boreal forest LAI, reflectance seasonality and species composition', *ISPRS Journal of Photogrammetry and Remote Sensing*. doi: 10.1016/j.isprsjprs.2013.01.001.

[8] Jones, H. G., & Vaughan, R. A. (2010). *Remote sensing of vegetation: principles, techniques, and applications*. Oxford, Oxford University Press. p. 384. ISBN 978–0–19–920779–4.

[9] Rautiainen, M. *et al.* (2018) 'Spectral properties of coniferous forests: A review of in situ and laboratory measurements', *Remote Sensing*. doi: 10.3390/rs10020207.

[10] Specim, Spectral Imaging Ltd. (2019) 'Specim IQ, Hyperspectral Goes Mobile', *website*. Available online: [http://www.specim.fi/iq/]. Accessed on: January 16 2019.

[11] Specim, Spectral Imaging Ltd. (2019) 'Specim, Spectral Imaging', *website*. Available online: [http://www.specim.fi/]. Accessed on: May 23, 2019.

[12] Behmann, J. *et al.* (2018) 'Specim IQ: Evaluation of a new, miniaturized handheld hyperspectral camera and its application for plant phenotyping and disease detection', *Sensors (Switzerland)*. doi: 10.3390/s18020441.

[13] Schaepman-Strub, G. *et al.* (2006) 'Reflectance quantities in optical remote sensing-definitions and case studies', *Remote Sensing of Environment*. doi: 10.1016/j.rse.2006.03.002.

[14] Roy, P. S. (1989) 'Spectral reflectance characteristics of vegetation and their use in estimating productive potential', *Proceedings: Plant Sciences*. doi: 10.1007/BF03053419.

[15] Lukeš, P. *et al.* (2013) 'Optical properties of leaves and needles for boreal tree species in Europe', *Remote Sensing Letters*. doi: 10.1080/2150704X.2013.782112.

[16] Nicodemus, F., Richmond, J. and Hsia, J. (1977) 'Geometrical considerations and nomenclature for reflectance', *Science And Technology*. doi: 10.1109/LPT.2009.2020494.

[17] Roosjen, P. P. J. *et al.* (2012) 'A laboratory goniometer system for measuring reflectance and emittance anisotropy', *Sensors (Switzerland)*. doi: 10.3390/s121217358.

[18] Shell, J. R. (2004) 'Bidirectional Reflectance : An Overview with Remote Sensing Applications & Measurement Recommendations', *Technical Report*: *Rochester Insitute of Technology Center for Imaging Science.*

[19] Wierzbicki, D. *et al.* (2018) 'Quality Assessment of the Bidirectional Reflectance Distribution Function for NIR Imagery Sequences from UAV', *Remote Sensing*. doi: 10.3390/rs10091348.

[20] Kuusk, A. (1991) 'The Hot Spot Effect in Plant Canopy Reflectance', in *Photon-Vegetation Interactions*. doi: 10.1007/978-3-642-75389-3_5.

[21] Myneni, R. B. *et al.* (1995) 'Optical remote sensing of vegetation: Modeling, caveats, and algorithms', *Remote Sensing of Environment*. doi: 10.1016/0034-4257(94)00073-V.

[22] Sandmeier, S. R. (2000) 'Acquisition of bidirectional reflectance factor data with field goniometers', *Remote Sensing of Environment*. doi: 10.1016/S0034-4257(00)00102-4.

[23] Labsphere, Inc. 'Optical-grade Spectralon® Reflectance Material', *Product Catalog*. Available online: [https://www.labsphere.com/site/assets/files/1827/pb-13021-000_rev_03_og_spectralon.pdf]. Accessed on: June 19, 2019.

[24] Suomalainen J. et al. (2009) 'Measurement and Analysis of Bidirectional Reflectances', *Seminario: Avances En Espectro-Radiometria.* Seminar presentation. Available online: [http://www.congresos.cchs.csic.es/seminarioradiometria/sites/congresos.cchs.csic.es.seminarioradiometria/files/Conferencia_7_Juha_Suomalainen_0.pdf]. Accessed on: June 19, 2019.

[25] Georgiev, G. T. and Butler, J. J. (2007) 'Long-term calibration monitoring of Spectralon diffusers BRDF in the air-ultraviolet', *Applied Optics*. doi: 10.1364/ao.46.007892.

[26] Malvern Panalytical Ltd. (2019) 'ASD range: Visible, NIR (and SWIR) spectrometers and spectroradiometers', *Product Catalog*. Available online: [https://www.malvernpanalytical.com/en/products/product-range/asd-range]. Accessed on: June 10, 2019.

[27] Spectra Vista Corporation (2019), 'Spectra Vista Corporation', *website.* Available online: [https://www.spectravista.com/]. Accessed on: June 24, 2019.

[28] Spectral Evolution Inc. (2019), 'Full Range/High Resolution Field Portable Spectroradiometers for Remote Sensing', *website.* Available online: [https://spectralevolution.com/products/hardware/field-portable-spectroradiometers-for-remote-sensing/]. Accessed on: June 24, 2019.

[29] Ocean Optics Inc. (2019), 'Ocean Optics', *website.* Available online: [https://oceanoptics.com/]. Accessed on: June 1, 2019.

[30] Cubert GmbH (2019), 'Cubert, Real-Time Spectral Imaging', *website*. Available online: [https://cubert-gmbh.com/]. Accessed on: May 25, 2019.

[31] Bruker (2019), 'Bruker', *website*. Available online: [https://www.bruker.com/]. Accessed on: May 25, 2019.

[32] Boreman, G. D. (2005) 'Classification of imaging spectrometers for remote sensing applications', *Optical Engineering*. doi: 10.1117/1.1813441.

[33] Aasen, H. *et al.* (2018) 'Quantitative remote sensing at ultra-high resolution with UAV spectroscopy: A review of sensor technology, measurement procedures, and data correctionworkflows', *Remote Sensing*. doi: 10.3390/rs10071091.

[34] Schopfer, Jürg; Dangel, S; Kneubühler, Mathias; Itten, Klaus I (2007). Dual field-of-view goniometer system FIGOS. In: ISPRS Working Group VII/1 Workshop ISPMSRS'07: "Physical Measurements and Signatures in Remote Sensing", Davos (CH), 12 March 2007 - 14 March 2007, 493-498.

[35] Dangel, S. *et al.* (2004) 'Combined field and laboratory goniometer system - FIGOS and LAGOS', in. doi: 10.1109/igarss.2003.1295536.

[36] Schopfer, J. T. *et al.* (2004) 'Comparison of field and laboratory spectro-directional measurements using a standard artificial target', in *Sensors, Systems, and Next-Generation Satellites VIII*. doi: 10.1117/12.585555.

[37] Odermatt, D. *et al.* (2005) 'Seasonal study of directional reflectance properties of snow', *EARSeL eProceedings*. 4(2): 203-214. doi: 10.5167/uzh-62131.

[38] Newport Corporation (2019), 'Oriel Instruments: Quartz Tungsten Halogen Lamps', *Product Catalog*. Available online: [http://www.spectroscopic.com/Oriel/63358.pdf]. Accessed on: June 3, 2019.

[39] Biliouris, D. *et al.* (2007) 'A Compact Laboratory Spectro-Goniometer (CLabSpeG) to assess the BRDF of materials. Presentation, calibration and implementation on Fagus sylvatica L. leaves', *Sensors*. doi: 10.3390/s7091846.

[40] Suomalainen, J. et al. (2008) 'Finnish Geodetic Institute Field Goniospectrometer (FIGIFIGO): A Device For Polarized Multiangular Reflectance, *Conference IGARSS 2008*, Conference Paper. Available online: [https://www.researchgate.net/publication/237222111_FINNISH_GEODETIC_INSTITUTE_FIELD_GONIOSPECTROMETER_FIGIFIGO_A_DEVICE_FOR_POLARIZED_MULTIANGULAR_REFLECTANCE_MEASUREMENTS]. Accessed on: May 24, 2019.

[41] Suomalainen, J. *et al.* (2009) 'Polarised multiangular reflectance measurements using the finnish geodetic institute field goniospectrometer', *Sensors*. doi: 10.3390/s90503891.

[42] Hakala, T., Suomalainen, J. and Peltoniemi, J. I. (2010) 'Acquisition of bidirectional reflectance factor dataset using a micro unmanned aerial vehicle and a consumer camera', *Remote Sensing*. doi: 10.3390/rs2030819.

[43] Forsström, P. *et al*. (2019) 'Seasonal dynamics of lingonberry and blueberry spectra', *Silva Fennica* 53. doi: 10.14214/sf.10150.

[44] Peltoniemi, J. I. *et al.* (2010) 'Land surface albedos computed from BRF measurements with a study of conversion formulae', *Remote Sensing*. doi: 10.3390/rs2081918.

[45] Roosjen, P. P. J., Bartholomeus, H. M. and Clevers, J. G. P. W. (2015) 'Effects of soil moisture content on reflectance anisotropy - Laboratory goniometer measurements and RPV model inversions', *Remote Sensing of Environment*. doi: 10.1016/j.rse.2015.09.022.

[46] Roosjen, P. *et al.* (2015) 'Investigating BRDF effects based on optical multi-angular laboratory and hyperspectral UAV measurements', in. doi: 10.1364/fts.2015.jm3a.15.

[47] Nolet, C. *et al.* (2014) 'Measuring and modeling the effect of surface moisture on the spectral reflectance of coastal beach sand', *PLoS ONE*. doi: 10.1371/journal.pone.0112151.

[48] Kawasaki Robotics (USA), Inc. (2019) 'F series High-Speed High-Performance Industrial Robots', *Product Catalog*. Available online: [https://techbrew.com/docs/FSeries.pdf]. Accessed on: May 10, 2019.

[49] Verrelst, J. *et al.* (2010) 'Effects of woody elements on simulated canopy reflectance: Implications for forest chlorophyll content retrieval', *Remote Sensing of Environment*. doi: 10.1016/j.rse.2009.11.004.

[50] Malenovský, Z. *et al.* (2008) 'Influence of woody elements of a Norway spruce canopy on nadir reflectance simulated by the DART model at very high spatial resolution', *Remote Sensing of Environment*. doi: 10.1016/j.rse.2006.02.028.

[51] Williams, D. L. (1991) 'A comparison of spectral reflectance properties at the needle, branch, and canopy level for selected Conifer species', *Remote Sensing of Environment*. doi: 10.1016/0034-4257(91)90002-N.

[52] Bousquet, L. *et al.* (2005) 'Leaf BRDF measurements and model for specular and diffuse components differentiation', *Remote Sensing of Environment*. doi: 10.1016/j.rse.2005.07.005.

[53] Thuillier, G. *et al.* (2003) 'The solar spectral irradiance from 200 to 2400 nm as measured by the SOLSPEC spectrometer from the ATLAS and EURECA missions', *Solar Physics*. doi: 10.1023/A:1024048429145.

[54] Thuillier, G. *et al.* (2003) 'The solar spectral irradiance from 200 to 2400 nm as measured by the SOLSPEC spectrometer from the ATLAS and EURECA missions', *Solar Physics*. doi: 10.1023/A:1024048429145. Available online: [https://oceancolor.gsfc.nasa.gov/docs/rsr/f0.txt]. Accessed on: March 15, 2019.

[55] Kwor, E. T. and Matteï, S. (2001) ‘Emissivity measurements for Nextel Velvet Coating 811-21 between -36°c and 82°c’, *High Temperatures - High Pressures*. doi: 10.1068/htwu385.

[56] Lang, M., Kuusk, A., Nilson, T., Lükk, T., Pehk, M., and Alm, G. Reflectance spectra of ground vegetation in sub-boreal forests. *Web page*. Available on-line [http://www.aai.ee/bgf/ger2600/] from Tartu Observatory, Estonia. Accessed on: May 20, 2019

[57] Hall, F. G *et al.* (2012) ‘Biophysical, morphological, canopy optical property, and productivity data from the Superior National Forest’, *NASA Technical Memorandum 104568.*

[58] Campbell, S. A. and Borden, J. H. (2005) ‘Bark reflectance spectra of conifers and angiosperms: Implications for host discrimination by coniferophagous bark and timber beetles’, *Canadian Entomologist*. doi: 10.4039/N04-082.